Performance tradeoffs in scaling InAlAs/InGaAs/InP metal-semiconductor-metal (MSM) photodetectors

by

Akbar Moolji

Submitted to the Department of Electrical Engineering and Computer Science
in partial fulfillment of the requirements for the degree of

Master of Science in Electrical Engineering

at the

MASSACHUSETTS INSTITUTE OF TECHNOLOGY

May 1995

© Massachusetts Institute of Technology 1995. All rights reserved.

MASSACHUSETTS INSTITUTE OF TECHNOLOGY

JUL 17 1995

LIBRARIES Barker Eng

Author ....
Department of Electrical Engineering and Computer Science
May 12, 1995

Certified by ....
Jesús A. del Alamo
Associate Professor of Electrical Engineering
Thesis Supervisor

Certified by ....
Henry I. Smith
Professor of Electrical Engineering
Thesis Supervisor

Accepted by ....
Frederic R. Morgenthaler
Chairman, Departmental Committee on Graduate Students

Performance tradeoffs in scaling InAlAs/InGaAs/InP metal-semiconductor-metal (MSM) photodetectors

by

Akbar Moolji

Submitted to the Department of Electrical Engineering and Computer Science
on May 12, 1995, in partial fulfillment of the
requirements for the degree of
Master of Science in Electrical Engineering

Abstract

Planar metal-semiconductor-metal (MSM) photodetectors have become an increasingly attractive choice for the front-end of integrated, high-performance optoelectronic receivers. For long-distance communication applications, it is essential that these devices be optimized for effective operation at the minimum dispersion and attenuation wavelengths (1.3 and 1.55 μm, respectively) of silica optical fibers. Consequently, we have focused our study on InAlAs/InGaAs/InP photodetectors.

We have developed a new set of conformal mappings that yields an analytical expression for the electric field in MSM photodetectors, correctly accounting for Fermi level pinning at the exposed semiconductor surface. Predictions based on this model were found to compare extremely well with results obtained from a 2-D Poisson simulator. A far-field approximation of this field distribution was used to develop an expression for the transit time of carriers generated within the photoabsorbing InGaAs layer. This, in turn, has been utilized in understanding the tradeoff between the 3 dB bandwidth and the quantum efficiency of the device.

We have also fabricated InAlAs/InGaAs/InP MSM photodetectors. Using image-reversal and lift-off techniques, we have optically patterned devices with finger widths and spacings down to 1 μm. In addition to this, we have used X-ray lithography to fabricate detectors with a minimum feature size of 0.3 μm. Both these sets of devices were found to have anomalous I-V characteristics. The questionable quality of the starting material is suspected to be responsible for this behavior.

The conclusions drawn from our study should prove useful in establishing correct design criteria for MSM photodetectors in the future.

Thesis Supervisor: Jesús A. del Alamo
Title: Associate Professor of Electrical Engineering

Thesis Supervisor: Henry I. Smith
Title: Professor of Electrical Engineering

Acknowledgments

First and foremost, I want to thank Prof. Jesùs del Alamo for his guidance throughout this project. Working with him, first as an undergraduate and now as a graduate student, has been a truly rewarding experience. I genuinely appreciate the role that he has played in my professional growth.

I sincerely thank Prof. Hank Smith for funding this effort and for permitting the usage of his lab facilities.

I have enjoyed my interactions with all the other members of the group, and would like to take this opportunity to wish them the best of luck with their respective careers.

My family has been very supportive all along. Their love and affection has time and again helped me through the toughest of situations. I want to thank my parents, in particular, for taking such a keen interest in my personal development. I hope they feel that their hard work has paid off!

Finally, I want to thank my jaan, Salima. Life would be meaningless without her.

Contents

1 Introduction **9**

1.1 Motivation 9

1.2 Thesis Goal and Outline 13

2 Electric field distribution in MSM structures **15**

2.1 Background 15

2.2 MSM detectors without Fermi level pinning 17

2.3 MSM detectors with Fermi level pinning 19

2.4 Far-field approximation 25

2.5 An alternative approach 29

2.6 Summary 32

3 Speed and efficiency of MSM photodetectors **33**

3.1 Overview 33

3.2 Transit-time limited response of MSM structures 33

3.2.1 The concept of displacement current 34

3.2.2 Transit-time of photogenerated carriers 36

3.2.3 Path length of a photocarrier 41

3.2.4 Displacement current in MSM structures 41

3.3 Quantum efficiency of MSM structures 45

3.4 Design tradeoffs for MSM photodetectors 46

3.5 Impact of Fermi level pinning on f_{3dB} 49

3.6 Summary 51

4 Technology for InAlAs/InGaAs MSM photodetectors **52**

4.1 Overview 52

4.2 Device design 52

4.3 Brief fabrication sequence 54

4.4 Measurement setup 57

4.5 Results and discussion 58

4.6 Summary 61

5 Conclusion **62**

A Potential distribution in III-V semiconductor based MSM photodetectors **64**

B 2D Poisson simulations **67**

C InGaAs/InP MSM Photodiode Process Sequence **70**

List of Figures

1-1 Block diagram of an optoelectronic receiver. 10

1-2 A schematic illustration of the structure and principle of operation of an MSM photodetector. 11

2-1 Schematic view of an MSM photodetector indicating the key device dimensions that affect the electric field within the structure. 16

2-2 Field distribution for a unit cell in an MSM structure without Fermi level pinning at the semiconductor surface. 18

2-3 The set of conformal mappings used by Gvozdić et al. to map the elementary cell into a parallel plate geometry. 19

2-4 Field distribution for an elementary cell in an MSM photodetector with Fermi level pinning at the exposed semiconductor surface. 20

2-5 Set of four conformal mappings that transforms the unit cell into a simple parallel plate structure. 22

2-6 2-D field maps for (a) L = d = 0.1 μm, and (b) L = 0.5 μm, d = 0.3 μm at V = 10 volts. 24

2-7 Cross-sections of the predicted and simulated fields for L = d = 0.1 μm and V = 10 volts, at x = 0, L/2 and (L+d)/2. 26

2-8 A far field approximation of the field distribution obtained by the method of conformal mapping for L = d = 0.1 μm at V = 10 volts. . 27

2-9 Plot of F(L/d) indicating how the discrepancy between the models grows as L/d is increased. 28

2-10 A qualitative explanation of why Gvozdić et al.'s analysis overestimates the field in III-V semiconductor based MSM photodetectors. 32

3-1 Schematic description of the physical origin of displacement current. . 34

3-2 Schematic cross-section of an MSM photodetector illustrating the definition of path length in these structures. 36

3-3 Velocity-field curves for carriers in InGaAs. Inset shows the piecewise linear velocity-field curves used in our analysis to estimate the transient behavior of electrons. 42

3-4 (a) Temporal response of a photodetector with L = d = 1 μm, at V = 10 volts, with the electron and hole contributions shown separately, and (b) the corresponding power spectra. 44

3-5 Schematic representation of the effects that limit the external quantum efficiency of an MSM photodetector. 45

3-6 The f_{3dB} and η_{ext} plots for L = d = 1 μm, and L = 2d = 2 μm at V = 10 volts. In each case, the active layer thickness, t_a, was assumed to be 1, 2 and 3 μm. 47

3-7 A parallel analysis of the f_{3dB} and η_{ext} tradeoff using the far-field approximation of Gvozdić et al.'s expression. Exaggerated 3 dB power bandwidths illustrate the importance of the Fermi-level pinning boundary condition. 47

3-8 Results highlighting the impact of Fermi level pinning. 50

4-1 Schematic cross-section of the target MSM photodetector. 53

4-2 The process flow. 55

4-3 An InAlAs/InGaAs/InP MSM photodetector with 1 μm wide fingers and spacings, that was fabricated at TRL, MIT. 56

4-4 SEM micrograph of an MSM photodetector with 0.3 μm wide fingers and spacings. The detector fingers were patterned with X-ray lithography. 56

4-5 Schematic view of the experimental setup designed to characterize the MSM detectors. 57
4-6 Typical I-V characteristics of an MSM photodetector. 58
4-7 Anomalous I-V characteristics exhibited by the fabricated devices. . . 59
4-8 DCXRD data for the heterostructure. 60

A-1 Boundary conditions along y = 0 65

B-1 Simulated structure. 68

Chapter 1

Introduction

1.1 Motivation

Novel applications can be realized by coupling the innate advantages of optics with the merits of electronic devices. OptoElectronic Integrated Circuits (OEICs) provide a unique way of harnessing this combined potential of optical and electronic components. The promise of this technology is evident in optical communication and computing systems. The optical interconnects used in these units, for example, outperform their conventional electrical counterparts. They permit high speed data transmission (at several tens of gigabits/s) over a large frequency range. This reduces the overall size and power consumption of the system and provides increased fan-out capabilities. The transmissions, themselves, are kept virtually free of possible corruptions from mutual interference and talkover, and the system stays unhampered by capacitive loading effects [1], [2]. With such outstanding features, common belief is that OEICs are destined to play a significant role in the field of communications. The possibility of commercial opportunities, that would follow as a result, has sparked a keen interest in this area and has led to numerous research efforts over the past two decades.

At the heart of an optical communication system lies a receiver. Its basic function is to detect and convert the incoming optical signal to an electrical pulse, such that the contents of the original transmission are retained. The main components of a

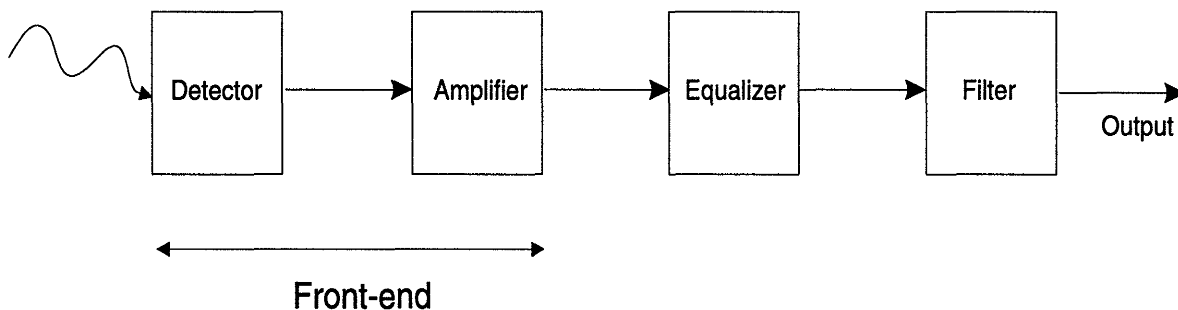

Figure 1-1: Block diagram of an optoelectronic receiver.

receiver that perform these tasks are shown in Fig 1-1. The front-end, which is comprised of the photodetector and the preamplifier, accomplishes the optical to electrical conversion and initial amplification of the resulting electrical signal. The equalizer and filter, that follow, perform pulse-shaping and other gain control tasks [1], [2].

The front-end critically determines the overall performance of the receiver. Designing a complete unit with a high bandwidth and sensitivity therefore translates to stringent performance criteria for both the preamplifier and the photodetector. The amplifier circuit, for example, must provide a significant noise-free output gain to allow effective recovery of relatively weak signals. In addition to this, its parasitics and leakage currents must also be minimized. Both field effect and bipolar junction transistors are generally used for this stage of the system.

The photodetector, for its part, must exhibit a high-speed and low-noise performance. This requires both a low capacitance and a small response time. Furthermore, for efficient optical to electrical conversion, the detector must have a high quantum efficiency and should not be plagued by excessive dark currents. Lastly, its structure should permit easy integration with the amplifier circuit [1].

Of all the choices available today, the metal-semiconductor-metal (MSM) photodetector best satisfies the requirements outlined above. As shown in Fig 1-2, this device consists of a set of interdigitated electrodes deposited on a photoabsorbing

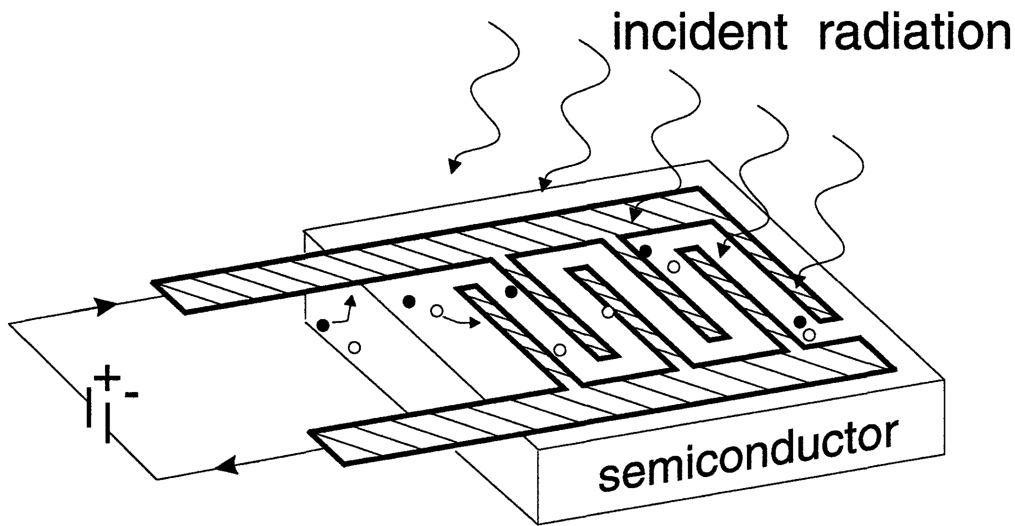

Figure 1-2: A schematic illustration of the structure and principle of operation of an MSM photodetector.

semiconductor layer. Radiation impinging on the photoactive layer creates electron hole pairs within it. A potential difference applied across the electrodes generates the field required to sweep out these photocarriers, and subsequently depletes the underlying semiconductor layer. The movement of these carries in turn alters the charge distribution on the metal fingers of the detector. The corresponding flow of charge in the external circuit produces an electrical signal (i.e. the displacement current) at the electrodes.

With its lateral, planar structure an MSM photodetector exhibits an extremely low capacitance when the underlying semiconductor is depleted under regular bias conditions. For a given light sensitive area, the capacitance of an MSM structure is therefore nearly four times smaller than that of a PIN diode [1]. An MSM detector with 1 μm wide fingers and a 2 μm interelectrode spacing, for example, has a capacitance of 1.5 fF/(10μm)^2. With a typical active area of 50 μm $\times$ 50 μm, this yields an external circuit (RC) charging time of about 1.9 ps for a 50 Ω active load [3]. Such behavior is highly desirable for achieving low-noise and high-speed performance.

The growing trend towards monolithic integration of optoelectronic circuits is another key reason for an increase in the popularity of the MSM photodetector. Its planar structure makes it highly compatible with the FET process. Hence the monolithic integration of an MSM photodiode and an FET can be achieved without introducing any additional process steps. The vertical structure of a PIN diode, in contrast, does not lend such a high degree of compatibility with the planar FET process. Even though a number of novel techniques, such as bridge interconnection [4], surface polishing for planarization [5], and a graded step process [6] have been examined to overcome this incompatibility, each one of them requires additional effort. MSM structures, with their intrinsic compatibility, are clearly a more attractive alternative.

As a result of their numerous advantages, MSM photodetectors have become an integral component in many optical communication systems [7]-[11]. Consequently, devices fabricated from a wide variety of materials, including Si [12]-[14], GaAs [15]-[17] and InGaAs [18]-[20] have been extensively studied and evaluated for their speed and sensitivity.

The choice of material for the active layer of an MSM photodetector depends on the application in mind. With light wave communication systems advancing towards data transmission rates over 10 GBits/s, ultrafast photodiodes operating in the 0.8 to 1.6 μm wavelength region are becoming the center of attraction. The development of ultrashort optical pulse sources, and the continued improvement in electrical sampling systems have further increased the demand for optoelectronic converters operating at several tens of GHz [21].

Such high speed performance can be achieved by using a GaAs or InGaAs photoactive layer. GaAs MSM photodetectors, for instance, have performed outstandingly in the short wavelength region ($\sim$ 0.8 μm). Zeghbroeck et al. have demonstrated a working device with a response frequency of 105 GHz [17]. Other efforts have successfully yielded integrated receivers comprising of GaAs MSM photodetectors and FET amplifiers that operate at high speed and sensitivity levels. The technology associated with GaAs has itself matured considerably over the years. GaAs-based MSM

receivers are therefore expected to monopolize the market for applications, such as local area networks and computer interconnects, that require optical links over short distances [1].

For long distance communications, however, optical transmission must be conducted at the minimum dispersion and attenuation wavelengths of silica optic fibers; 1.3 and 1.55 μm respectively [22]. As a result, the narrow bandgap InGaAs has been under investigation as an alternative material for the photoactive layer. In addition to having a high cut-off wavelength, InGaAs enjoys other advantages over GaAs, namely a higher low-field mobility [23] and higher saturation and peak electron velocities [24]. These properties, in principle, should yield MSM photodetectors with a superior speed performance. InGaAs-based MSM photodetectors can therefore prove to be viable candidates for long wavelength optical communication applications.

1.2 Thesis Goal and Outline

As noted earlier, *speed* and *sensitivity* are the two most important figures of merit of an MSM photodetector. The intrinsic speed of these detectors is limited by the transit time of photogenerated carriers. This is largely determined by the electric field within the structure, and is therefore directly dependent on the geometry of the device, i.e. the finger width, the finger spacing and the thickness of the active layer. These factors also affect the sensitivity of the detector. Hence the key to designing high speed, high sensitivity photodetectors lies in understanding the exact nature of these dependencies.

The primary objective of this thesis was to understand how these critical device dimensions affect the performance of $In_{0.53}Ga_{0.47}As$ MSM photodetectors on a semi-insulating InP substrate. Unlike other such studies, the device model used in our work is more accurate since it incorporates the Fermi level pinning boundary condition that is typically observed in III-V compound semiconductors. As shown later in the thesis, this correction is crucial for establishing proper design criteria for MSM detectors fabricated from this material system.

The outline of this thesis is as follows: In Chapter 2 a set of conformal mappings is presented that yields an analytic expression for the electric field distribution in III-V semiconductor based MSM photodetectors. This work is unique since it correctly accounts for Fermi level pinning at the exposed semiconductor surface. Predictions based on this model are validated by comparing them with results obtained from a 2D Poisson simulator. A far field approximation of this field distribution is compared with a study [25] that ignores the Fermi level pinning condition. This comparison highlights the importance of the boundary condition at the semiconductor surface. We then present an alternative method for determining the electric field in MSM structures. This approach provides greater insight into the differences that arise in the field distribution as a result of ignoring the Fermi level pinning condition.

In Chapter 3 the far field approximation is used to develop an expression for the transit time of photogenerated carriers. This in turn is utilized in numerically evaluating the temporal response, power spectrum and the associated 3 dB bandwidth for a variety of photodetector designs. We perform a comprehensive study of the tradeoff between the 3 dB bandwidth and the quantum efficiency of these detectors, for situations both with and without Fermi level pinning at the semiconductor surface.

Chapter 4 focuses on the experimental aspects of the thesis. In this section we present the details of fabricating and characterizing InGaAs/InP MSM photodetectors. In particular, we outline the process technology for realizing MSM detectors with sub-micron size fingers and spacings using X-ray lithography. The key conclusions of this thesis are summarized in Chapter 5.

Chapter 2

Electric field distribution in MSM structures

2.1 Background

In principle, the net response of an MSM photodetector is dependent both on the transit time of the photogenerated carriers and the RC charging time of the external circuit. With its planar interdigitated structure, however, an MSM photodiode enjoys the advantage of a relatively low parasitic capacitance [1]. Consequently, its temporal response is dominated by the carrier transit times. The motion of these carriers is in turn dictated by the electric field within the device. Hence a performance appraisal of the MSM photodetector requires an evaluation of the field distribution within the structure.

Figure 2-1 is the schematic view of an MSM photodiode with finger width d and interelectrode spacing L. Typically, a voltage V is applied across the two sets of interdigitated electrodes that lie on the photoactive semiconductor layer. The length of the fingers is generally much larger than their width. For all practical purposes, then, determining the field distribution for this structure amounts to solving Poisson's equation in two dimensions.

Two different approaches have been adopted traditionally to solve this problem. Those interested in accurately predicting the performance of MSM photodetectors

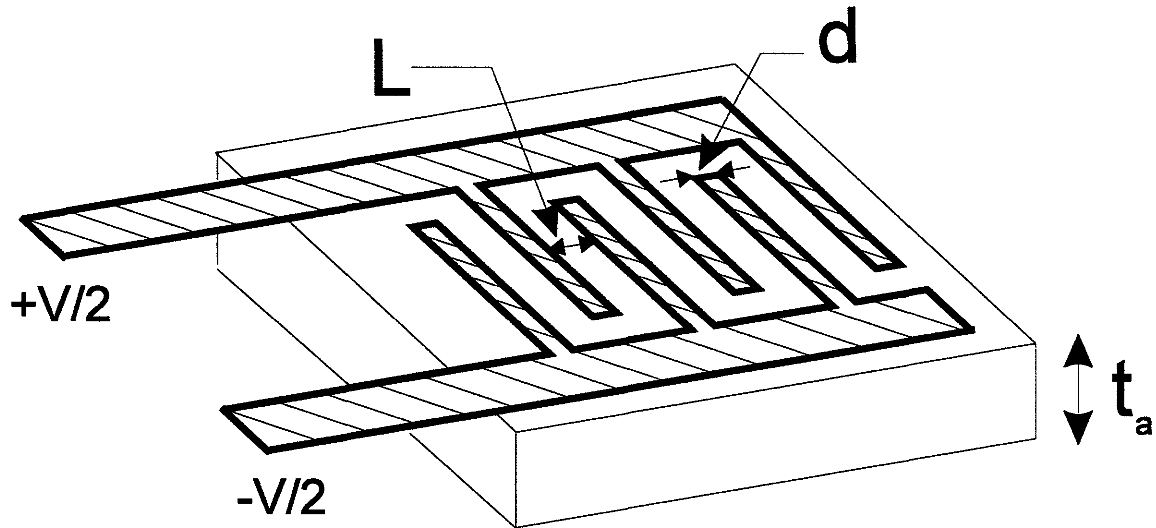

Figure 2-1: Schematic view of an MSM photodetector indicating the key device dimensions that affect the electric field within the structure.

operating at *both* low and high levels of light intensity, include the presence photogenerated carriers in their analysis. By solving Boltzmann's transport and Poisson's field equation self-consistently, these studies account for modifications to the field distribution due to the presence of free carriers. Both 1D [26] and 2D [27] self-consistent Monte Carlo simulations of this nature have been performed to determine how the response time and frequency bandwidth of MSM detectors scale with the dimensions of the device, the applied voltage and the excitation intensity.

At regular optical power levels, however, carrier concentrations are not sufficient to significantly alter the electric field resulting from the externally applied voltage. Complex computations involving self-consistent field solutions can therefore be avoided for many applications. In a classic paper, Lim and Moore [28] have solved a simplified two-dimensional problem in which they neglect the presence of photocarriers. Using the method of conformal mapping, the authors chart out the electric field lines and potential distribution for the periodic structure shown in Fig. 2-1. The results of their analysis have been used effectively by Soole and Schumacher [3] to provide insight

into the the transit-time limited behavior of InGaAs-based MSM photodetectors. The conformal mappings used by Lim and Moore, however, yield complex elliptic integrals of the first kind, and hence entail a laborious numerical evaluation of the electric field. Consequently, by using their results, Soole and Schumacher fail to provide analytical expressions that could prove useful in designing MSM photodetectors.

2.2 MSM detectors without Fermi level pinning

Recently, Gvozdić et al. [25] have used a new, more simple conformal mapping to obtain an analytical expression for the electric field in MSM photodetectors. Their work is outlined here.

In approaching the problem, the authors make the following assumptions (for context see Fig. 2-1):

- The photoactive layer is intrinsic, or weakly doped. Consequently, bulk carrier concentrations can be ignored.
- The thickness of photoabsorbing layer, t_a, is semi-infinite.
- The length of the electrode fingers is much larger than their width. This reduces the problem to two dimensions.
- The number of fingers is sizeable. Edge effects can therefore be overlooked.
- The metal electrodes have negligible thickness.

Given these assumptions, the electric field for the structure shown in Fig. 2-1 is periodic along the semiconductor surface, with a repetition period of (L+d). The authors note that it is therefore sufficient to evaluate the field for a single unit cell. Fig. 2-2 shows the distribution for one such cell, demarcated by the limits $-(L+d)/2 < x < (L+d)/2$, and $-\infty < y < \infty$. The boundary conditions for the problem are set by the externally applied voltage, V. Hence despite the difference in the dielectric constants of the semiconductor layer and air, the electric field is symmetric

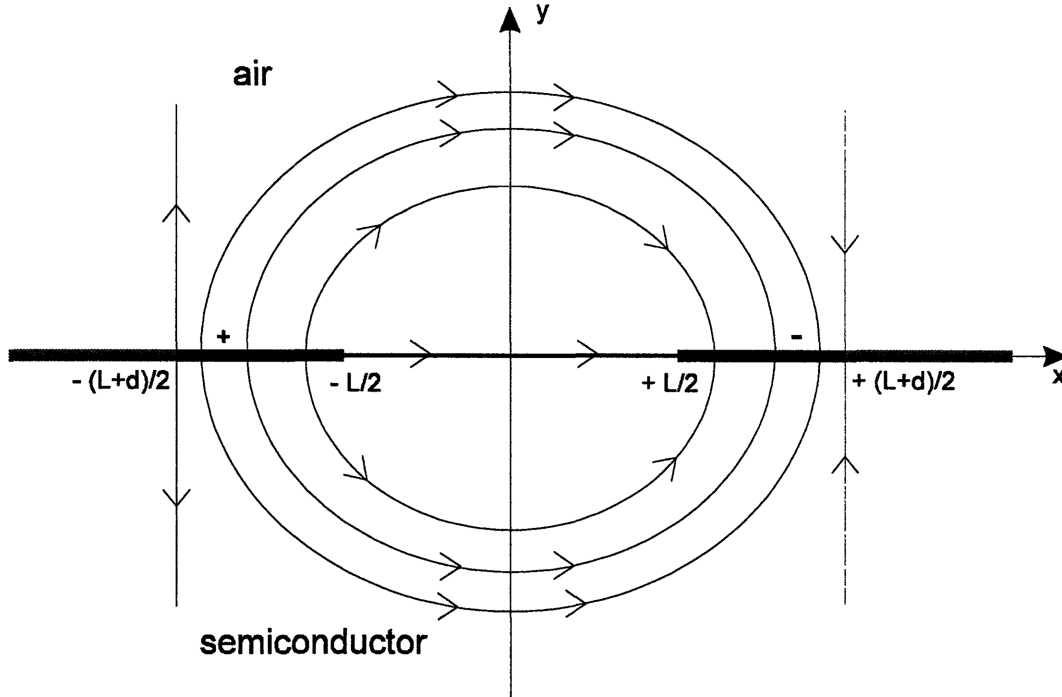

Figure 2-2: Field distribution for a unit cell in an MSM structure without Fermi level pinning at the semiconductor surface.

about the x-axis. According to Gvozdić et al., as a result of the symmetry of the problem, field lines emanating from the edges of the electrodes are coplanar with the semiconductor-vacuum boundary. Furthermore, since the y-axis is centered relative to the two electrodes, it forms an equipotential surface. The field lines are therefore perpendicular to it along its entire length.

Gvozdić et al. map the elementary cell shown in Fig. 2-2 into a simple parallel plate structure through a combination of two transforms, Fig. 2-3. The equipotential surfaces and the orthogonal field lines in the resulting geometry are then denoted respectively by:

$$u = Re(w) \tag{2.1}$$

$$v = Im(w) \tag{2.2}$$

Using the transforms the authors in turn determine an analytical expression for the

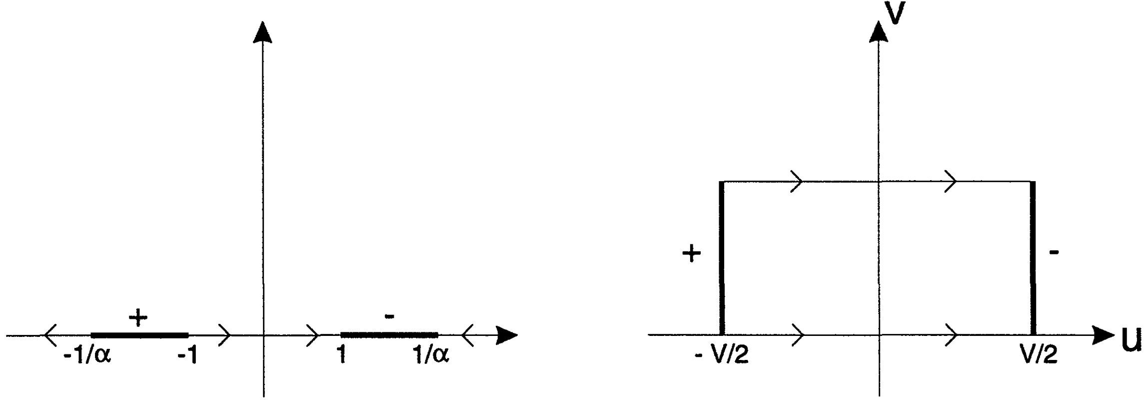

Figure 2-3: The set of conformal mappings used by Gvozdić et al. to map the elementary cell into a parallel plate geometry.

electric field:

$$|\mathcal{E}^*(x,y)| = \left[\frac{\pi V\sqrt{2}}{2(L+d)K(\alpha)}\right]\left[\left(cos\left(\frac{2\pi x}{L+d}\right)cosh\left(\frac{2\pi y}{L+d}\right) - cos\left(\frac{\pi L}{L+d}\right)\right)^2 + sin^2\left(\frac{2\pi x}{L+d}\right)sinh^2\left(\frac{2\pi x}{L+d}\right)\right]^{-\frac{1}{4}} \tag{2.3}$$

Here

$$K(\alpha) = \int_0^1 \frac{dx}{\sqrt{(1-\alpha^2)(1-\alpha^2 x^2)}} \tag{2.4}$$

with $\alpha = sin\frac{\pi L}{2(L+d)}$.

2.3 MSM detectors with Fermi level pinning

The problem considered by Gvozdić et al. permits the presence of electric field lines along the air-semiconductor interface that lies between two adjacent electrodes. In the case of III-V semiconductors, however, Fermi level pinning results in an equipotential air-semiconductor boundary between the detector fingers. Hence, the method

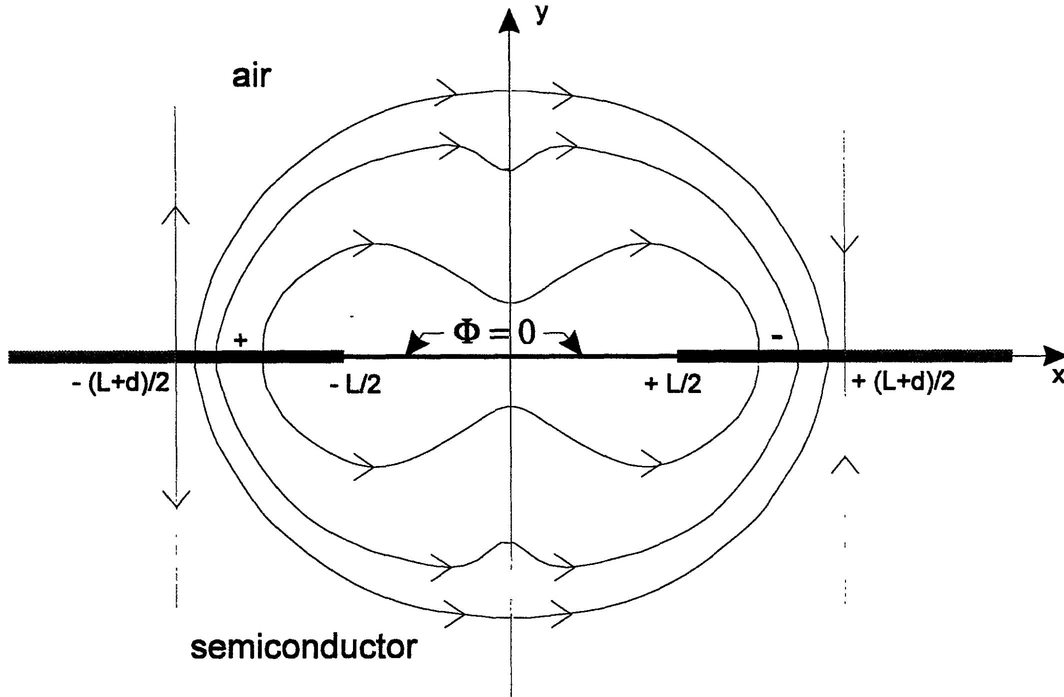

Figure 2-4: Field distribution for an elementary cell in an MSM photodetector with Fermi level pinning at the exposed semiconductor surface.

of Gvozdić et al. does not depict the physics of these structures accurately. Since both GaAs- and InGaAs-based receivers are crucial for short and long wavelength applications, it is imperative that a new calculation be carried out that correctly accounts for Fermi level pinning at the semiconductor surface. The set of conformal mappings presented in this section accomplishes this objective.

Referring back to Fig. 2-1, a pinned Fermi level implies that the entire interelectrode spacing, L, is fixed at a constant potential. If we arbitrarily set the voltages at the two electrodes to to $\pm$ V/2 volts, symmetry forces the exposed surface of the semiconductor to be maintained at $\Phi = 0$ volts. For simplicity, we will assume that the potential changes abruptly at the finger edges from 0 to $\pm$ V/2 volts. Making the same assumptions as Gvozdić et al., we notice that the field distribution in this case is also periodic. Once again, the repetition period is (L+d). Fig. 2-4 shows the distribution for an elementary cell which, not too surprisingly, has the same limits as the unit cell in Fig. 2-2. In this case, however, there are no field lines along

the equipotential air-semiconductor boundary. The center of the cell now lies at the intersection of two orthogonal equipotential surfaces. Hence the field at this point drops down to zero. Furthermore, as a result of the periodic nature of the structure, the field lines along $x = \pm$ (L+d)/2 are vertical over the entire range of values of y.

This unit cell can be mapped to the more familiar parallel plate geometry through a series of four conformal mappings (Fig. 2-5). The first of these mappings:

$$\beta(z) = sin\frac{\pi z}{L+d} \tag{2.5}$$

where $z = x + iy$, opens the air and semiconductor regions into semi-infinite half planes, Fig. 2-5(a). The field lines perpendicular to the electrodes at $x = \pm$ (L+d)/2 are mapped along the real axis under this transformation (see figure).

The second, and most important of the four transforms:

$$\chi(\beta) = \frac{\sqrt{\beta^2 - sin^2\frac{\pi L}{2(L+d)}}}{\sqrt{1 - sin^2\frac{\pi L}{2(L+d)}}} \tag{2.6}$$

collapses the spacing between the electrodes onto the imaginary axis. With the two electrodes ($\pm$ V/2) now placed head-to-head, Fig. 2-5(b), the 0 volts condition along the imaginary axis is automatically satisfied. Hence, it is perfectly legitimate to henceforth ignore the redundant interelectrode spacing that was mapped along the imaginary axis.

The third mapping in the series:

$$\nu(\chi) = \frac{1}{\chi} \tag{2.7}$$

separates and extends the electrodes out along the real axis to $\pm\infty$.

Finally,

$$w(\nu) = \frac{V}{\pi} sin^{-1}(\nu) \tag{2.8}$$

yields the requisite parallel plate geometry, Fig. 2-5(d).

These transforms can be used to obtain analytical expressions for the potential

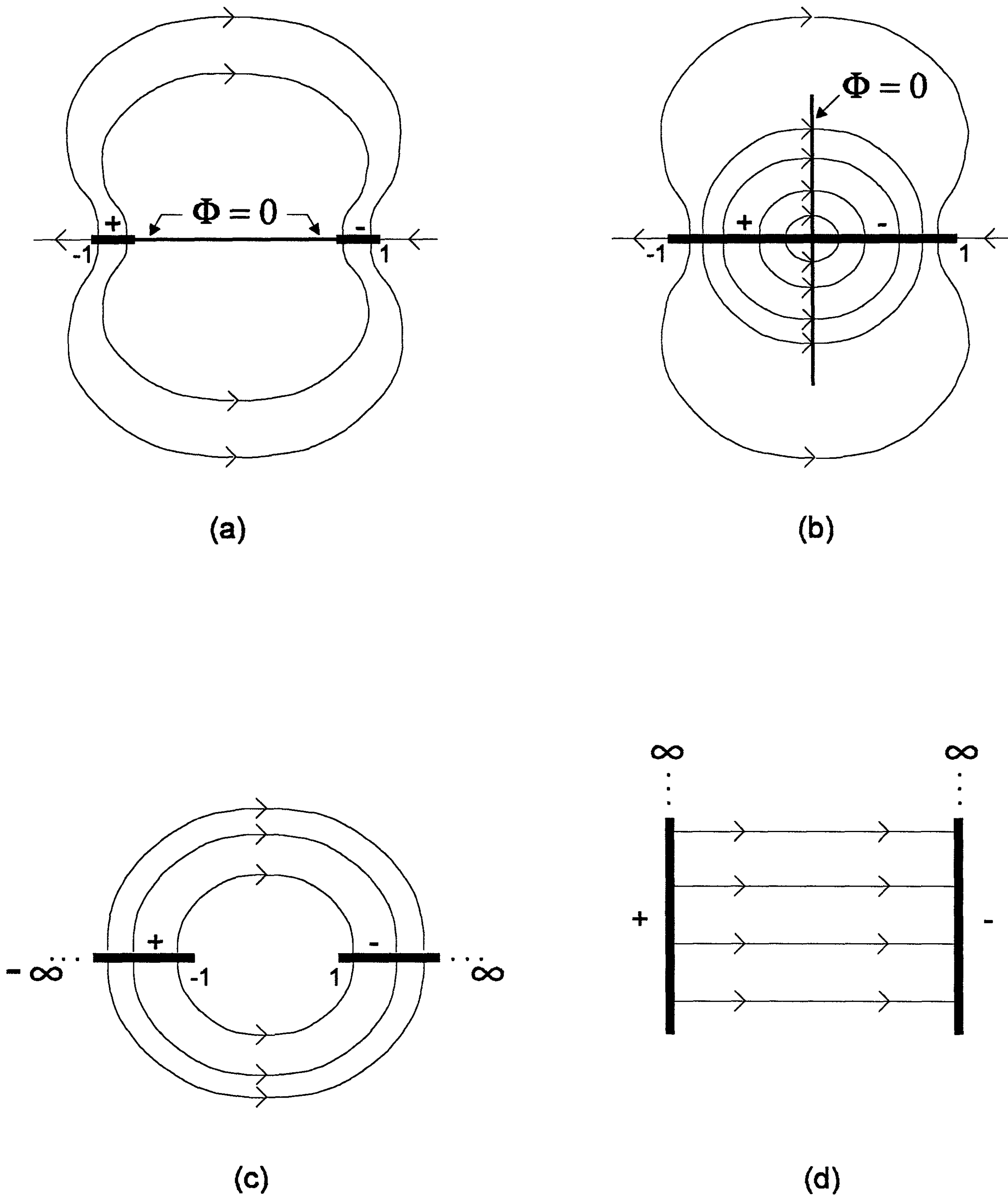

Figure 2-5: Set of four conformal mappings that transforms the unit cell into a simple parallel plate structure.

distribution, $\Phi(z)$, and the electric field, $\mathcal{E}(z)$. Hence,

$$\Phi(z) = \frac{V}{\pi} Re \left[sin^{-1} \frac{\sqrt{1 - sin^2 \frac{\pi L}{2(L+d)}}}{\sqrt{sin^2 \frac{\pi z}{L+d} - sin^2 \frac{\pi L}{2(L+d)}}} \right] \tag{2.9}$$

and

$$|\mathcal{E}(z)| = \left| \frac{dw}{dz} \right| = \frac{V \sqrt{1 - sin^2 \frac{\pi L}{2(L+d)}}}{L+d} \left| \frac{sin \frac{\pi z}{L+d}}{sin^2 \frac{\pi z}{L+d} - sin^2 \frac{\pi L}{2(L+d)}} \right| \tag{2.10}$$

where $z = x + iy$.

It is easy to verify that (2.9) satisfies the following boundary conditions at $y = 0$:

$$\Phi(z) = \begin{cases} 0 & \text{for} \quad 0 < |x| < L/2 \\ \pm V/2 & \text{for } L/2 < |x| < (L+d)/2 \end{cases}$$

Details of the proof are given in Appendix A.

At a glance, (2.10) also seems to have the correct functional form. It predicts that $|\mathcal{E}(0,0)| = 0$, which is consistent with our earlier observation that no field lines should pass through the center of the cell. Also, according to (2.10) $|\mathcal{E}(z)|$ diverges at z = (±L/2, 0). This is a restatement of our assumption that the potential changes abruptly at the edges of the detector fingers.

Given its complexity, the general features of the 2-D field map are best illustrated pictorially. Fig. 2-6(a) shows the field distribution for a unit cell with L = d = 0.1 μm, and V = 10 volts. From (2.10) above we know that $|\mathcal{E}(z)|$ blows up at the finger edges. To prevent this from masking some of the other features of the distribution, the field along the surface has been excluded from the figure. As expected, $|\mathcal{E}(z)|$ is symmetric about the $x = 0$ line. Close to the surface the electric field varies considerably along the x-direction, peaking directly below the finger edges. However, on moving further down into the semiconductor this variation disappears completely, and the field decays uniformly with the distance from the surface.

From a design perspective, it is essential to understand how this field map changes with the finger width and the interelectrode spacing. Fig. 2-6(b) shows the distribution for an arrangement in which a larger fraction of the unit cell is left unmetallized:

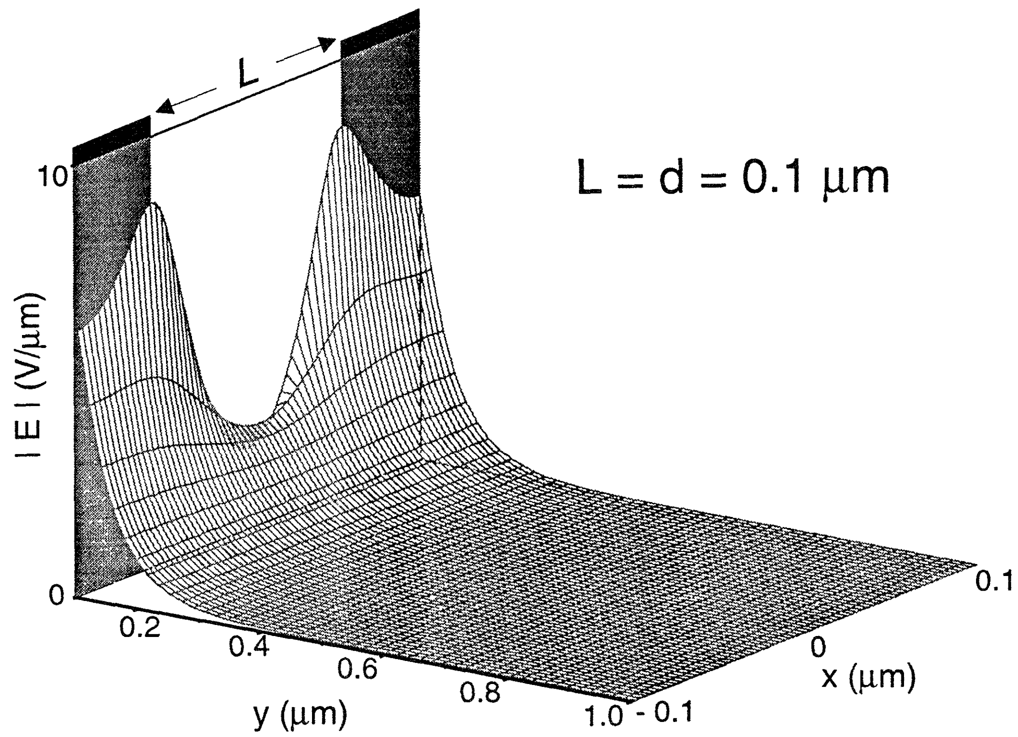

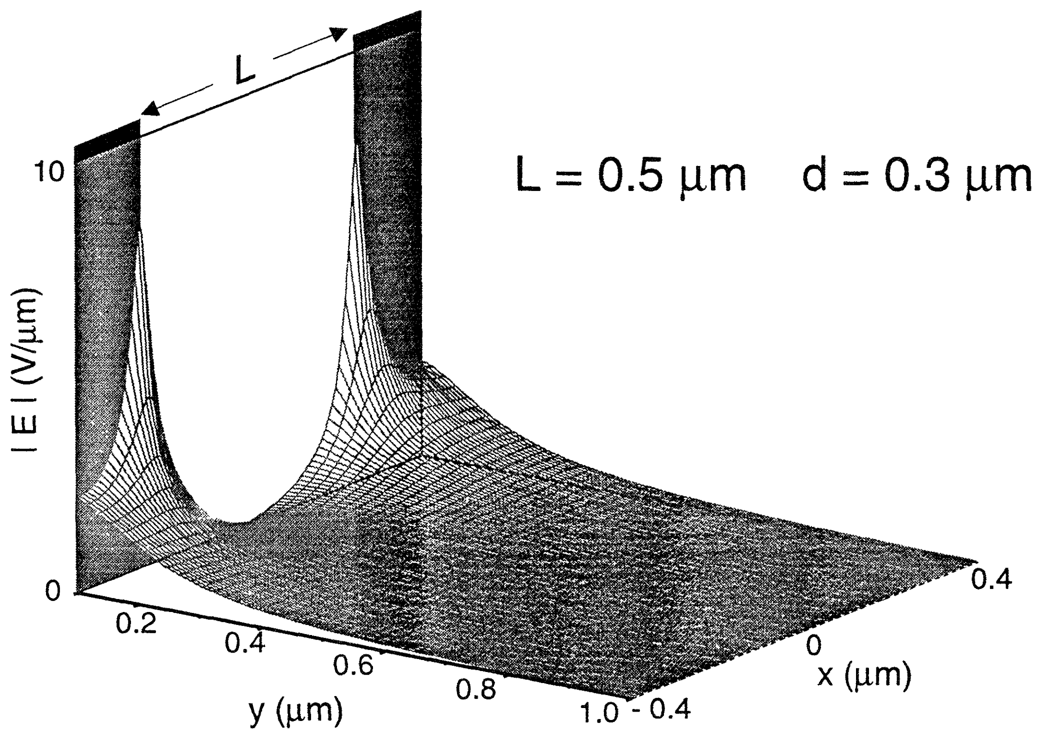

Figure 2-6: 2-D field maps for (a) L = d = 0.1 μm, and (b) L = 0.5 μm, d = 0.3 μm at V = 10 volts.

L = 0.5 μm, d = 0.3 μm with V = 10 volts. As compared to the L = d = 0.1 μm case, this geometry permits an extra 12% of the incident intensity to impinge on the photoactive layer. From a performance point of view, such a design would therefore yield a higher responsivity detector. The field distribution in this case, however, is notably different from that shown in Fig. 2-6(a). On the whole, $|\mathcal{E}(z)|$ has decreased everywhere. This is reasonable, since (2.10) predicts that the electric field gets scaled roughly by 1/(L+d). The finger edges are an obvious exception to this scaling. Since the field at these points is determined by the abrupt change in potential, it is independent of the geometry of the device. Again, just as before, the field map has structure close to the surface but decays uniformly on moving deeper into the semiconductor. Now, however, the field persists for comparatively larger values of y.

The validity of (2.10) was checked by comparing the field distribution predicted by it to that obtained from a 2-D Poisson simulator [1] that permits Fermi-level pinning at the exposed surface [29]. Fig. 2-7 shows cross-sectional plots of the predicted and simulated results for a unit cell with L = d = 0.1 μm, and V = 10 volts. At each of the three representative points, x = 0, L/2 and (L+d)/2, the results compare extremely well. The slight discrepancy in the two distributions is an artifact of the finite mesh size used for the 2-D simulation which precludes an abrupt potential change at the edges of the electrodes.

2.4 Far-field approximation

It was noted earlier that as y gets sufficiently large, the 2-D field becomes independent of x. This can be verified easily. In the limit $y \gg (L+d)/\pi$,

$$\left| sin\frac{\pi(x+iy)}{L+d} \right| \simeq \left| \frac{1}{2} e^{\frac{\pi y}{L+d}} \left(sin\frac{\pi x}{L+d} + i cos\frac{\pi x}{L+d} \right) \right| = \frac{1}{2} e^{\frac{\pi y}{L+d}} \gg 1 \qquad (2.11)$$

[1] See Appendix B for details of a typical simulation.

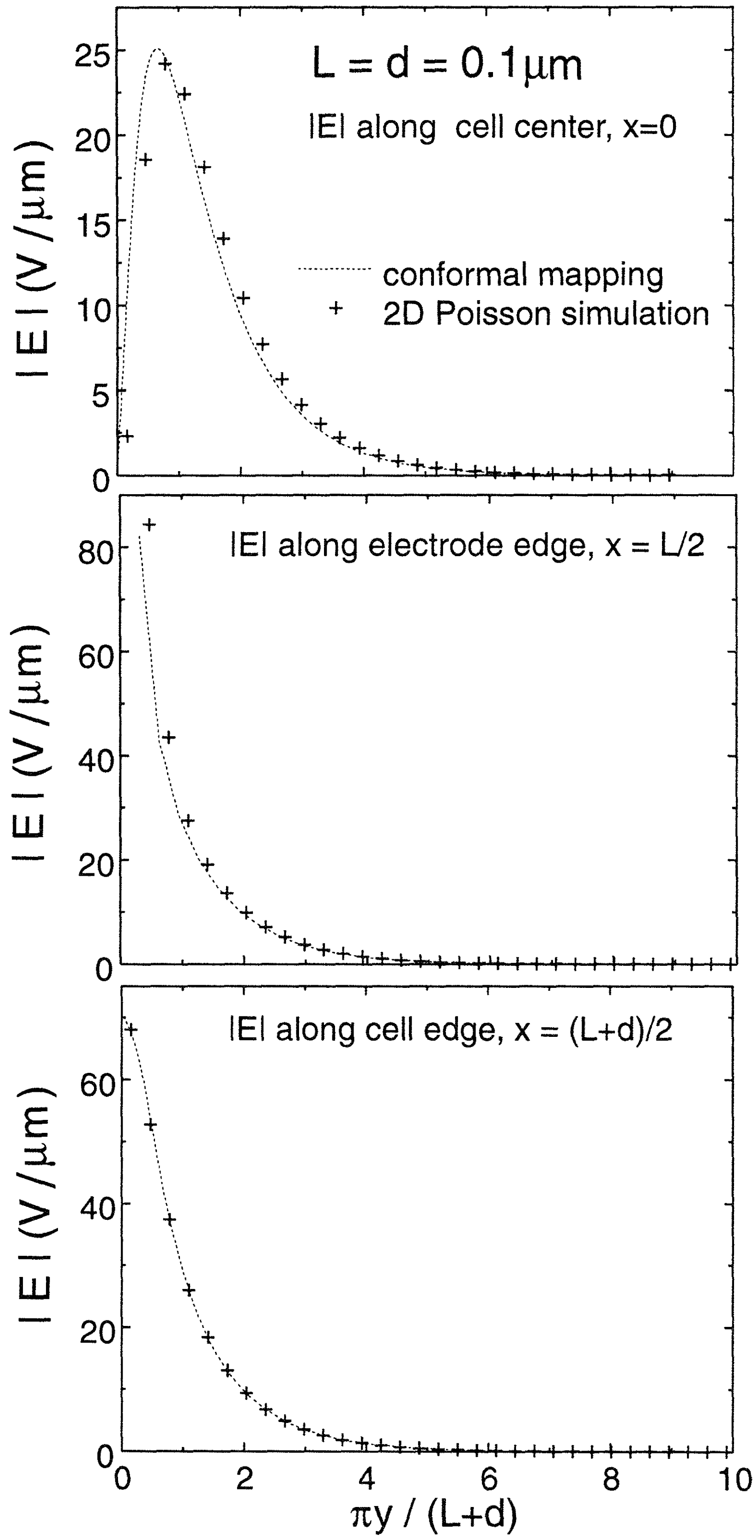

Figure 2-7: Cross-sections of the predicted and simulated fields for L = d = 0.1 μm and V = 10 volts, at x = 0, L/2 and (L+d)/2.

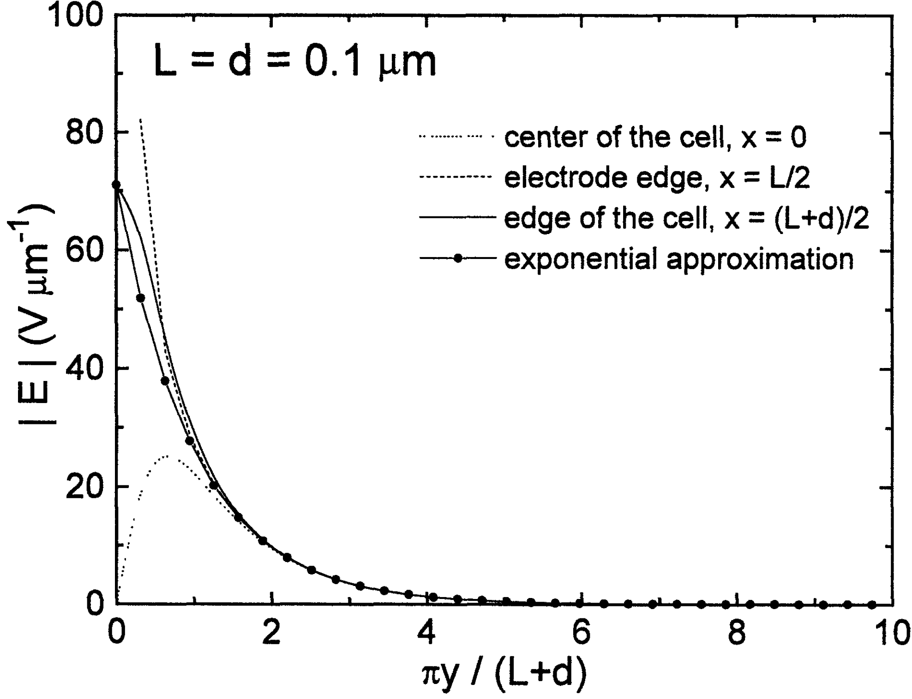

Figure 2-8: A far field approximation of the field distribution obtained by the method of conformal mapping for L = d = 0.1 μm at V = 10 volts.

Since $sin\frac{\pi L}{2(L+d)} \leq 1$, (2.11) implies that $\left|sin\frac{\pi z}{L+d}\right| \gg \left|sin\frac{\pi L}{2(L+d)}\right|$. Hence, in this far-field limit, (2.10) can be written as:

$$|\mathcal{E}(x,y)| \simeq \frac{2V\sqrt{1-sin^2\frac{\pi L}{2(L+d)}}}{L+d}e^{-\frac{\pi y}{L+d}} = \mathcal{E}_o e^{-\frac{\pi y}{L+d}} \tag{2.12}$$

Fig. 2-8 illustrates the accuracy of this far-field exponential form. Beyond $y \simeq$ (L+d)/π the exponential approximation closely follows the field distribution predicted by (2.10) for all values of x. In addition to this, (2.12) successfully captures the trade-off between the magnitude and the spatial extent of the electric field through the 1/(L+d) and the $e^{-\frac{\pi y}{L+d}}$ terms, respectively.

Interestingly, in the same limit the expression developed by Gvozdić et al. (2.3) also simplifies to a uniform exponential decay:

$$|\mathcal{E}^*(x,y)| \simeq \frac{V}{L+d}\frac{\pi}{K(\alpha)}e^{-\frac{\pi y}{L+d}} = \mathcal{E}_g e^{-\frac{\pi y}{L+d}} \tag{2.13}$$

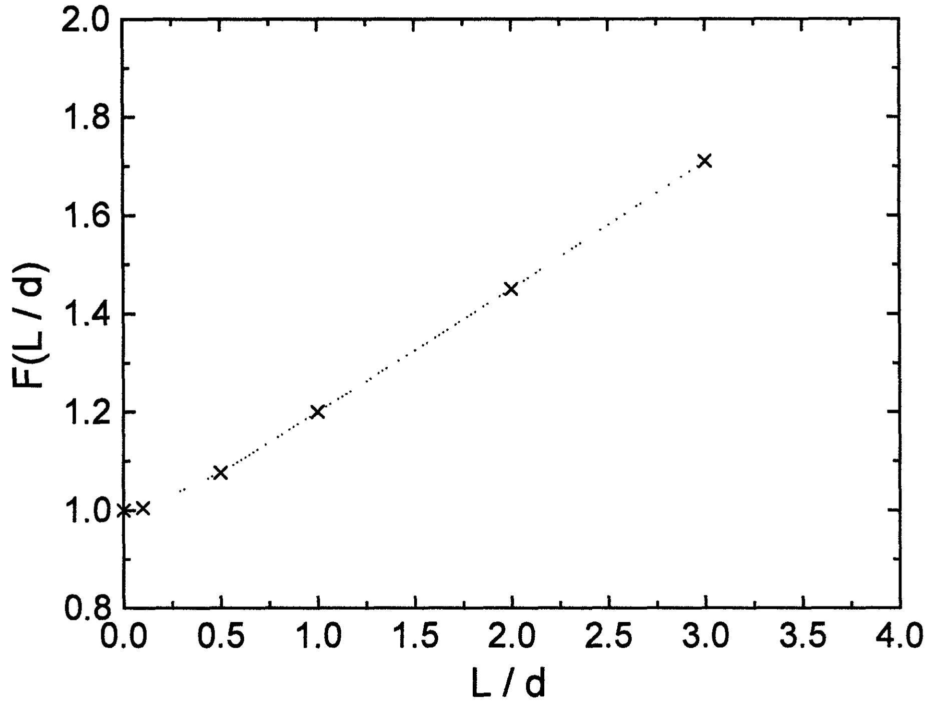

Figure 2-9: Plot of F(L/d) indicating how the discrepancy between the models grows as L/d is increased.

where $\mathcal{E}^*$ is the electric field in an MSM detector without Fermi level pinning at the semiconductor surface.

It is instructive to examine the ratio of the far-field expressions that result from Gvozdić et al.'s and our treatment of the problem. This ratio is found to be a constant that depends only on L/d:

$$F(L/d) = \frac{\mathcal{E}^*(x,y)}{\mathcal{E}(x,y)} = \frac{\pi}{2K(\alpha)\sqrt{1 - sin^2\frac{\pi L}{2(L+d)}}} \tag{2.14}$$

Fig. 2-9 is a plot of F(L/d) at selected values of L/d. With $L/d < 1$, F(L/d) stays close to unity. For this range of values the interelectrode spacing is small compared to the finger width and therefore the surface does not play a dominant role in determining the field distribution deep inside the semiconductor. As L/d is increased, the region with the Fermi level pinning boundary condition begins to occupy a larger fraction of the unit cell. Consequently, the discrepancy in the two field distributions grows. At $L/d = 2$, for example, the far-field limit of [25] overestimates the field in III-V

semiconductor-based MSM structures by nearly 45%. This observation is particularly important for detectors that are designed with large L/d ratios in order to achieve high responsivities. Applying Gvozdić et al.'s results to such structures will clearly yield inaccurate results.

2.5 An alternative approach

The electrostatic problem considered in the previous sections can be solved using an approach that provides more insight into the far-field approximations developed in Section 2.4. It is important to recall that determining the field distribution for an MSM structure essentially translates to solving Poisson's equation in two dimensions with appropriate boundary conditions. Specifically, for photodetectors with Fermi level pinning at the semiconductor surface we need to solve:

$$\frac{\delta^2\Phi(x,y)}{\delta x^2} + \frac{\delta^2\Phi(x,y)}{\delta y^2} = 0 \tag{2.15}$$

subject to the following boundary conditions:

1. $\Phi(x, y = 0) = 0$ for $0 < |x| <$ L/2
2. $\Phi(x, y = 0) =$ V/2 for -(L+d)/2 $< x <$ -L/2
3. $\Phi(x, y = 0) =$ -V/2 for L/2 $< x <$ (L+d)/2
4. $\Phi(|x| = L + d, y) = 0$
5. $\Phi(x, y) \to 0$ as $y \to \infty$

Using separation of variables, the partial differential equation above can be easily converted into a pair of ordinary differential equations:

$$\frac{d^2X}{dx^2} = -k^2X \tag{2.16}$$

$$\frac{d^2Y}{dy^2} = +k^2Y \tag{2.17}$$

where k is a constant, and X and Y are defined such that:

$$\Phi(x,y) = X(x)Y(y) \tag{2.18}$$

Both (2.16) and (2.17) have simple solutions:

$$X(x) = A\sin kx + B\cos kx \tag{2.19}$$

$$Y(y) = Ce^{ky} + De^{-ky} \tag{2.20}$$

where A, B, C and D are constants that need to be determined. Consequently, (2.18) can be rewritten as:

$$\Phi(x,y) = (A\sin kx + B\cos kx)(Ce^{ky} + De^{-ky}) \tag{2.21}$$

In order to determine the constants in (2.21), we need to use the boundary conditions enumerated earlier. To satisfy condition 5, we can immediately conclude that C = 0. Furthermore, it is clear from condition 1 that $\Phi(x,y)$ must drop down to zero at the origin of our coordinate system. This in turn implies that B = 0 also. Absorbing D into A, (2.21) simplifies to:

$$\Phi(x,y) = A\sin kx\, e^{-ky} \tag{2.22}$$

In addition to this, condition 4 requires that $sink(L+d) = 0$. Hence,

$$k = \frac{n\pi}{L+d} \tag{2.23}$$

where n = 1, 2, 3...

To satisfy the remaining conditions along $y = 0$, we need to exploit the linearity of Laplace's equation. As a result of this property, we are guaranteed that a linear com-

bination of terms similar to (2.22) will also yield a solution to (2.15). Superimposing these terms, we get:

$$\Phi(x,y) = \sum_k A_k \sin kx\, e^{-ky} \tag{2.24}$$

where the different values of k are specified by (2.23).

It is obvious from (2.24) that in the far field limit, as $y \to \infty$, the leading term with $k = \frac{\pi}{L+d}$ will dominate. The associated constant A can be obtained by invoking the orthogonality property of the $\sin kx$ terms in (2.24):

$$2\int_{-(L+d)/2}^{(L+d)/2} \Phi(x,0) \sin \frac{\pi x}{L+d}\, dx = A(L+d) \tag{2.25}$$

The integral above can be evaluated using boundary conditions 1, 2 and 3, which completely specify the form of $\Phi(x,0)$ over the interval of interest. After some algebra, we find that:

$$A = -\frac{2V}{\pi} \cos \frac{\pi L}{2(L+d)} \tag{2.26}$$

Consequently, in the far field limit:

$$\Phi(x,y) \simeq -\frac{2V}{\pi} \cos \frac{\pi L}{2(L+d)} \sin \frac{\pi x}{L+d} e^{-\frac{\pi y}{L+d}} \tag{2.27}$$

From (2.27) we can in turn obtain a far field expression for $|\mathcal{E}(x,y)|$:

$$|\mathcal{E}(x,y)| \simeq \frac{|A|\,\pi}{L+d} e^{-\frac{\pi y}{L+d}} = \frac{2V}{L+d} \cos \frac{\pi L}{2(L+d)} e^{-\frac{\pi y}{L+d}} \tag{2.28}$$

Using the trigonometric identity, $\cos a = \sqrt{1-\sin^2 a}$, (2.28) can be rewritten as:

$$|\mathcal{E}(x,y)| \simeq \frac{2V\sqrt{1 - sin^2 \frac{\pi L}{2(L+d)}}}{L+d} e^{-\frac{\pi y}{L+d}} \tag{2.29}$$

This is exactly the far field expression that was obtained in the previous section.

This alternative approach can be used to qualitatively understand why Gvozdić et al.'s treatment of the problem overestimates the field in MSM structures with Fermi

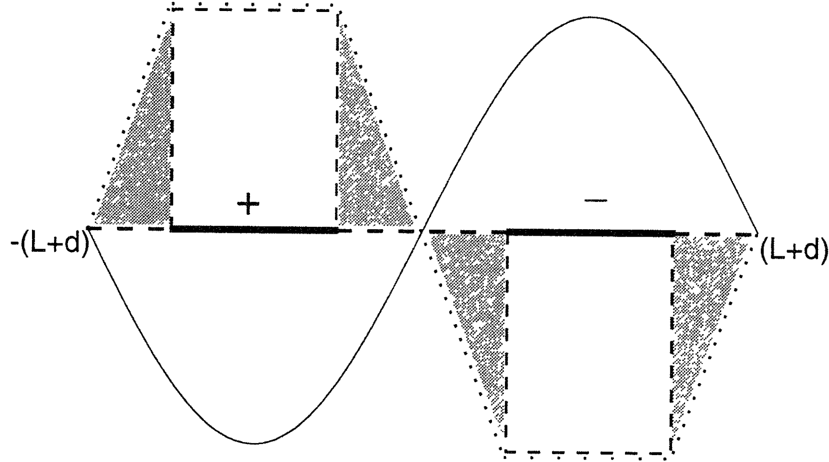

Figure 2-10: A qualitative explanation of why Gvozdić et al.'s analysis overestimates the field in III-V semiconductor based MSM photodetectors.

level pinning at the semiconductor surface. In our analysis above, we found that $|A|$ is determined by the extent of overlap between the $\sin \frac{\pi x}{L+d}$ and the $\Phi(x, 0)$ terms. Fig. 2-10 shows the potential distributions, along $y = 0$, that were assumed in Gvozdić et al.'s and our evaluation of the electric field. Clearly, with the extra overlap (denoted by the shaded regions in the figure), $|A|$ is greater if the Fermi level pinning boundary condition is ignored. From (2.28) it follows that the corresponding field distribution will also be artificially amplified.

2.6 Summary

Using a new set of conformal mappings, we have derived an analytical expression for the field distribution in MSM photodetectors with Fermi level pinning at the semiconductor surface. We have subsequently shown that ignoring this boundary condition leads to an overestimation of the electric field strength in these devices. The discrepancy grows with the L/d ratio, and becomes significant for designs aimed at achieving high responsivity detectors.

Chapter 3

Speed and efficiency of MSM photodetectors

3.1 Overview

The performance of an MSM photodetector is typically evaluated in terms of its speed and quantum efficiency. As with most figures of merit, however, a strong tradeoff exists between these two performance measuring benchmarks. In the present chapter we quantify this tradeoff for typical photodetector designs. We examine cases both with and without Fermi level pinning at the semiconductor surface. Our analysis indicates that in order to correctly assess the performance of III-V semiconductor based MSM detectors, it is necessary to account for the Fermi level pinning condition.

3.2 Transit-time limited response of MSM structures

The temporal response of an MSM photodetector is a critical figure of merit in many communications applications. Since an MSM structure generally has small external parasitics, this response is limited primarily by the motion of photogenerated carriers. In order to ascertain the transient behavior of an MSM detector, it is

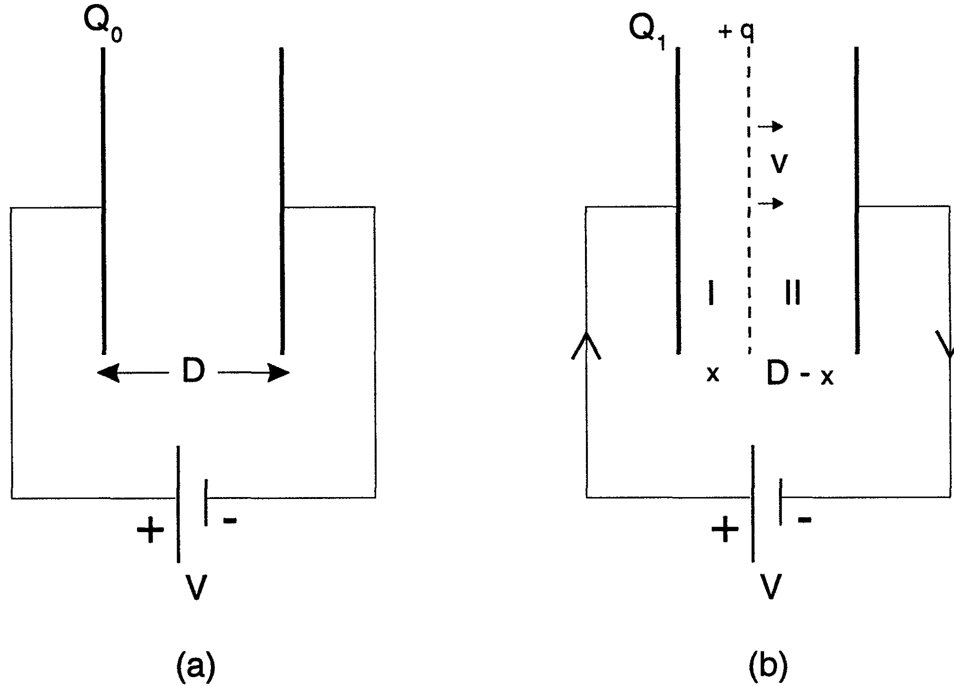

Figure 3-1: Schematic description of the physical origin of displacement current.

therefore necessary to evaluate the displacement current recorded at the metal fingers as a result of the flow of photocarriers within the structure [30].

3.2.1 The concept of displacement current

Consider the simple case shown in Fig. 3-1a, in which a constant potential difference, V, is maintained across two metal electrodes of surface area A. Suppose the charge on the two plates is $\pm Q_o$. The electric field in the region in between them is simply $Q_o/(\epsilon A)$, where ϵ is the permittivity of the enclosed medium. If D is the separation between the plates, it follows that:

$$\frac{Q_o D}{\epsilon A} = V \tag{3.1}$$

Suppose now a thin sheet, with total charge q spread over a surface area A, is inserted between these plates at a distance x from the left electrode (see Fig. 3-1b). As this sheet moves towards the right plate, the original distribution of charges on the two electrodes will get altered such that the net potential drop across the structure

is always V. The corresponding flow of charge in the external circuit constitutes the displacement current.

This current can be easily evaluated in terms of the parameters shown in Fig. 3-1. Let us assume that at a given instant, after the insertion of the sheet, the charge on the left plate is denoted by Q_1. The electric fields in regions I and II (see Fig. 3-1b) are simply:

$$\begin{aligned} \mathcal{E}_I &= \frac{Q_1}{\epsilon A} \\ \mathcal{E}_{II} &= \frac{Q_1 + q}{\epsilon A} \end{aligned} \tag{3.2}$$

Since the potential drop between the two plates is fixed at V,

$$\frac{Q_1 x}{\epsilon A} + \frac{(Q_1 + q)(D - x)}{\epsilon A} = V \tag{3.3}$$

Equating (3.1) and (3.3) above, we can solve for Q_1:

$$Q_1 = (Q_o - q) + \frac{qx}{D} \tag{3.4}$$

The displacement current, $I(t)$, is in turn given by:

$$I(t) = \frac{dQ_1}{dt} = \frac{qv}{D} \tag{3.5}$$

where v is the instantaneous velocity of the drifting sheet. It is important to note that this current is recorded in the external circuit only so long as the sheet of charge is in motion. Once the sheet gets collected at the right plate, $I(t)$ instantaneously drops to zero.

The simple analysis outlined above can be used to compute the impulse response of an MSM detector. Analogous to the charged sheet in the case above, each photogenerated carrier will contribute to the total current until it is finally collected at one of the electrodes. The contribution made by such a carrier at any given instant

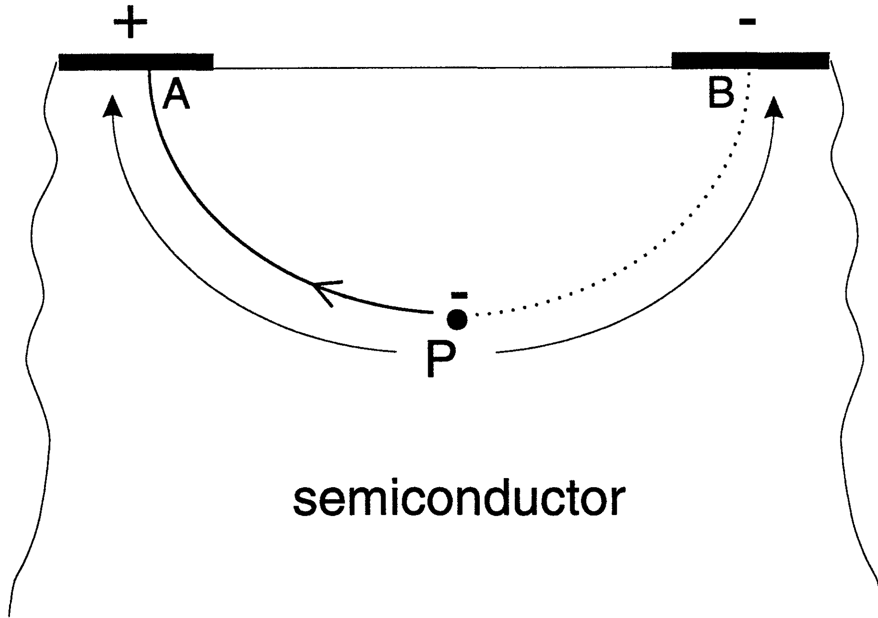

Figure 3-2: Schematic cross-section of an MSM photodetector illustrating the definition of path length in these structures.

is in essence captured by (3.5), except in this case D, the spacing between the metal plates, takes on a new interpretation. As shown in Fig. 3-2, it instead corresponds to the total length, P, of a carrier's trajectory. Hence each carrier essentially "sees" a different effective distance between the metal electrodes.

In order to compute the temporal response of an MSM photodetector it is therefore necessary to evaluate both the transit time and the path length associated with each photogenerated carrier. This task is accomplished in the following sections.

3.2.2 Transit-time of photogenerated carriers

For a carrier generated at $(x_o,\ y_o)$, the transit time is simply:

$$\tau(x_o, y_o) = \int_{y_o}^{0} \frac{dy}{v_y} = \int_{x_o}^{x_f} \frac{dx}{v_x} \tag{3.6}$$

where x_f is the x-coordinate of the point-of-collection, and v_x and v_y are the x and y components of the carrier's velocity at each point along its path. We chose to perform

the above integral along the x-direction. This entailed determining x_f and v_x for each carrier.

For a given (x_o, y_o), the corresponding x_f can be obtained easily once the trajectory of the carrier is known. Since these carriers move along field lines whose x and y components are given by:

$$\mathcal{E}_x(x,y) = -Re\left[\frac{dw}{dz}\right] \tag{3.7}$$

and

$$\mathcal{E}_y(x,y) = Im\left[\frac{dw}{dz}\right] \tag{3.8}$$

the differential equation governing their motion is:

$$\frac{dy}{dx} = \frac{\mathcal{E}_y}{\mathcal{E}_x} = -\frac{Im\left[\frac{dw}{dz}\right]}{Re\left[\frac{dw}{dz}\right]} \tag{3.9}$$

Integrating (3.9) above, and setting y = 0 in the result should yield x_f.

The exact form of v_x, on the other hand, depends on whether the carrier's motion is mobility-limited or velocity-saturated. In the mobility-limited mode,

$$v_x = \pm\ \mu\mathcal{E}_x \tag{3.10}$$

where μ, depending on the type of carrier in question, is the electron or hole mobility. On entering the velocity-saturation regime, the carrier velocity becomes independent of the electric field strength. Since the carriers continue to move along the field lines, their motion is still in the direction described by (3.9). Now, however,

$$v_x = \pm\ v_{sat,x} = \pm\ \vec{v}_{sat}.\hat{x} \tag{3.11}$$

where $v_{sat,x}$ is the projection of the carrier's saturation velocity, $\vec{v}_{sat}$, along the x-direction.

In the most general case, a carrier could start off in the mobility limited regime

deep within the active layer where the field is weak, and then eventually attain saturation velocity as it drifts towards the electrodes into regions where the field is stronger. The transit time for such a carrier can be computed in two steps. Since (3.10) applies to the mobility-limited leg of the trajectory, it can first be used in conjunction with (3.6) and (3.9) to determine the time that elapses before the carrier reaches velocity-saturation. In this case, then, x_f takes on a new interpretation. Now, instead, it represents the point of transition between the mobility-limited and the velocity-saturation regimes. Using this as the starting point for the second half of the motion, and substituting (3.11) in (3.6) then yields the time spent by the carrier in velocity-saturation before it is finally collected.

For carriers limited to a single mode of transport, the transit time calculation would be similar in essence to that stated above. For such cases, however, the *entire* motion would be depicted by either the mobility-limited or the velocity-saturation regime equations.

To make this analysis tractable, we decided to use the far-field approximation, which estimates the field distribution beyond $y \simeq (\mathrm{L+d})/\pi$ extremely well. Since slow moving holes generated deep within the semiconductor layer tend to limit the temporal response of an MSM photodetector, this simplification is reasonable.

Under this approximation, (3.7) and (3.8) become:

$$\mathcal{E}_x(x,y) = \mathcal{E}_o e^{-\frac{\pi y}{L+d}} cos\frac{\pi x}{L+d} \tag{3.12}$$

and

$$\mathcal{E}_y(x,y) = -\mathcal{E}_o e^{-\frac{\pi y}{(L+d)}} sin\frac{\pi x}{L+d} \tag{3.13}$$

With these expressions, (3.9) simplifies to:

$$\frac{dy}{dx} = -tan\frac{\pi x}{L+d} \tag{3.14}$$

On integrating (3.14), the trajectory followed by the carriers is found to be:

$$y = \frac{L+d}{\pi} ln \left| cos\frac{\pi x}{L+d} \right| - \frac{L+d}{\pi} ln \left| cos\frac{\pi x_o}{L+d} \right| + y_o \tag{3.15}$$

Setting $y = 0$ in (3.15) above, we finally get:

$$x_f = \frac{L+d}{\pi} cos^{-1} \left(e^{-\frac{\pi y_o}{L+d}} cos\frac{\pi x_o}{L+d} \right) \tag{3.16}$$

To account for carrier motion both in the mobility-limited and velocity-saturation regimes, transit time expressions were developed separately for each of these modes of transport, as summarized below.

(i) Mobility-limited transport.

Substituting (3.12) into (3.10) yields:

$$v_x = \mu \mathcal{E}_o e^{-\frac{\pi y}{L+d}} cos\frac{\pi x}{L+d} \tag{3.17}$$

Using (3.15) above, it is easy to see that for this regime (3.6) simplifies to:

$$\tau(x_o, y_o) = \frac{(x_f - x_o)\, e^{\frac{\pi y_o}{L+d}}}{\mu \mathcal{E}_o cos\frac{\pi x_o}{L+d}} \tag{3.18}$$

where $\mathcal{E}_o$ is given by (2.12) and x_f by (3.16). A parallel treatment of (2.13) yields the transit time for carriers in MSM photodetectors without Fermi level pinning. The final result differs from (3.18) only in that $\mathcal{E}_o$ gets replaced by $\mathcal{E}_g$.

The key dependencies depicted in (3.18) make intuitive sense. According to it, carriers generated deeper within the photoactive layer (at larger values of y_o, for a given x_o) stay in transit longer. This can be attributed both to an increase in the net distance covered by the carriers (notice, x_f increases with y_o) and to the weaker fields that they experience deep inside the active layer (captured by the exponential term). Similarly, increasing L, in an attempt to achieve higher-responsivity devices, also translates to longer transit times. The effects are once again two fold: a reduced $\mathcal{E}_o$, and a larger x_f.

(ii) Velocity-saturation regime.

Using (3.11), in this case

$$v_x = v_{sat} \, cos \frac{\pi x}{L+d} \tag{3.19}$$

where v_{sat} is the saturation velocity of the carrier.

Consequently, the transit time for this regime is found to be:

$$\tau(x_o, y_o) = \frac{L+d}{\pi v_{sat}} \, ln \left| \frac{sec\frac{\pi x_f}{L+d} + tan\frac{\pi x_f}{L+d}}{sec\frac{\pi x_o}{L+d} + tan\frac{\pi x_o}{L+d}} \right| \tag{3.20}$$

(iii) General case.

If a carrier's motion is limited to only one of the two regimes, the transit time is given by either (3.18) or (3.20). On the other hand, for carriers that start off in the mobility-limited mode but reach velocity-saturation before being collected, (3.18) and (3.20) must be used together to compute the net transit time. For such a general case,

$$\tau = \tau_{mob} + \tau_{sat} \tag{3.21}$$

where τ_{mob} and τ_{sat} are the times spent by the carrier in the mobility-limited and velocity-saturation regimes respectively.

We can easily develop an explicit expression for this net transit time. Let $\mathcal{E}_{sat}$ be the critical field at which a carrier hits velocity saturation. Hence, regions of the unit cell under mobility-limited and velocity-saturated modes of transport are separated by the line:

$$y_{sat} = \frac{L+d}{\pi} \, ln \left(\frac{\mathcal{E}_o}{\mathcal{E}_{sat}} \right) \tag{3.22}$$

Substituting (3.22) into (3.15) we can find the corresponding x-coordinate, x_{sat}, at which a given carrier crosses this line:

$$x_{sat} = \frac{L+d}{\pi} \, cos^{-1} \left[\frac{\mathcal{E}_o}{\mathcal{E}_{sat}} e^{-\frac{\pi y_o}{L+d}} cos \frac{\pi x_0}{L+d} \right] \tag{3.23}$$

Combining (3.18) and (3.20), (3.21) above can be rewritten as:

$$\tau(x_o, y_o) = \frac{(x_{sat} - x_o)\, e^{\frac{\pi y_o}{L+d}}}{\mu \mathcal{E}_o cos\frac{\pi x_o}{L+d}} + \frac{L+d}{\pi v_{sat}}\, ln\left|\frac{sec\frac{\pi x_f}{L+d} + tan\frac{\pi x_f}{L+d}}{sec\frac{\pi x_{sat}}{L+d} + tan\frac{\pi x_{sat}}{L+d}}\right| \tag{3.24}$$

3.2.3 Path length of a photocarrier

Referring back to Fig. 3-2, the path length associated with a photogenerated carrier is given by:

$$P = \int_{AtoB} ds \tag{3.25}$$

Using $ds = \sqrt{(dx)^2 + (dy)^2}$, (3.25) can be converted to an integral along the x- direction. Hence,

$$P = 2\int_0^{x_f} \sqrt{1 + \left(\frac{dy}{dx}\right)^2}\, dx \tag{3.26}$$

Furthermore, we know from Chapter 2 that

$$\frac{dy}{dx} = -tan\frac{\pi x}{L+d} \tag{3.27}$$

Substituting this into (3.26) above and evaluating the integral, we find that:

$$P = \frac{2(L+d)}{\pi v_{sat}}\, ln\left|sec\frac{\pi x_f}{L+d} + tan\frac{\pi x_f}{L+d}\right| \tag{3.28}$$

3.2.4 Displacement current in MSM structures

Having developed expressions for the transit time and the path length associated with each carrier, we can now evaluate the total displacement current, $I(t)$ at any given instant. This simply amounts to numerically summing the individual contributions of carriers that are still in motion within the active layer at that time. The result can in turn be used to calculate the power spectrum, $P(\omega)$, and the associated 3 dB bandwidth, f_{3dB}, from the simple relationship: $P(\omega) = |\mathcal{F}[I(t)]|^2$.

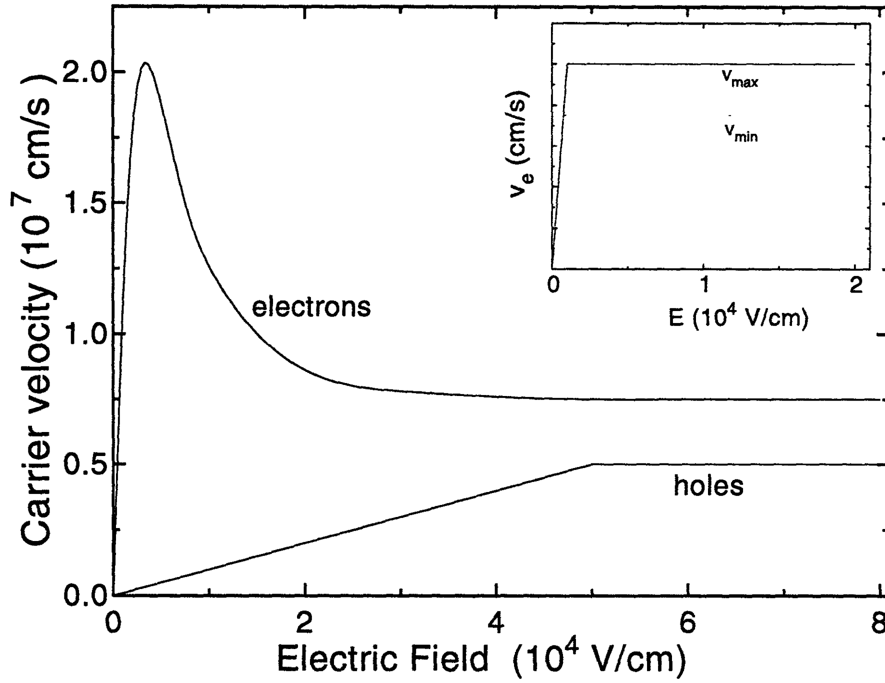

Figure 3-3: Velocity-field curves for carriers in InGaAs. Inset shows the piecewise linear velocity-field curves used in our analysis to estimate the transient behavior of electrons.

Before proceeding, it is important to note that (3.24) accounts for the general case only if carrier velocities follow a piecewise linear velocity-field relationship. Fig. 3-3 shows the actual velocity-field curves for electrons and holes in InGaAs [31]. Quite clearly, our assumption does not impose any limitations on tracking the time evolution of holes, even though it does rule out a precise analysis in the case of electrons. As noted in [21], however, the bandwidth of an MSM detector is determined primarily by the dynamics of the holes. Hence, as long as f_{3dB} is the parameter of interest, our inability to model the motion of electrons accurately should not yield misleading results.

We therefore assumed a simple linear velocity-field relationship for electrons. In order to approximate the peak in the actual electron velocity-field curves, we performed two calculations for each given combination of detector geometry and externally applied voltage: one with the electron saturation velocity, $v_{e,sat}$, set at v_{min} and another with $v_{e,sat} = v_{max}$ (see inset to Fig 3-3). The values of v_{min} and v_{max} were

chosen such that they allowed us to best bracket the transient behavior of electrons. For L = d = 1 μm and V = 10 volts, for example, an active layer thickness of 1 μm results in $|\mathcal{E}(x, y)| \geq 1.5 \times 10^4$ V/cm. In this case, then, the electron velocity lies approximately between 7.5×10^6 and 1×10^7 cm/s over the entire photoabsorbing thickness. Hence, $v_{min} = 7.5 \times 10^6$ cm/s and $v_{max} = 1 \times 10^7$ cm/s are the appropriate choices.

Fig 3-4a shows the temporal response for the sample case outlined above, in which the saturation velocity of electrons was assumed to be 1×10^7 cm/s. The initial carrier distribution, for this case, was computed in response to a light pulse of $\lambda = 1.55$ μm, which corresponds to an optical penetration length, L_λ, of 1.47 μm [3]. The metal electrodes were assumed to be opaque. Hence initially the carriers were limited to -L/2 < x < L/2 for all values of y. The issue of a finite active layer thickness was handled in a way similar to [3]. The photoabsorbing InGaAs layer was taken to lie on a semi-insulating InP substrate. Even though in reality the electric field lines in such a structure would penetrate into the InP, carrier motion was confined to the InGaAs layer only. Carriers reaching the InGaAs/InP interface were limited to motion along it such that their trajectories were symmetric about the $x = 0$ axis.

It is obvious from Fig. 3-4a that the temporal response of the detector has two distinct components to it. The rapid decay, seen initially, results from fast moving electrons that get collected within the first 20 ps. The long tail, on the other hand, is caused by the slower holes. The corresponding power spectra are shown in Fig. 3-4b. The 3 dB bandwidth for the net response was found be 17.5 GHz. Interestingly, the individual spectra for the electron and hole displacement currents had 3 dB bandwidths of 35 GHz and 10 GHz, respectively. These values justify the remark made earlier that the detector bandwidth is mainly dependent on the dynamics of the holes.

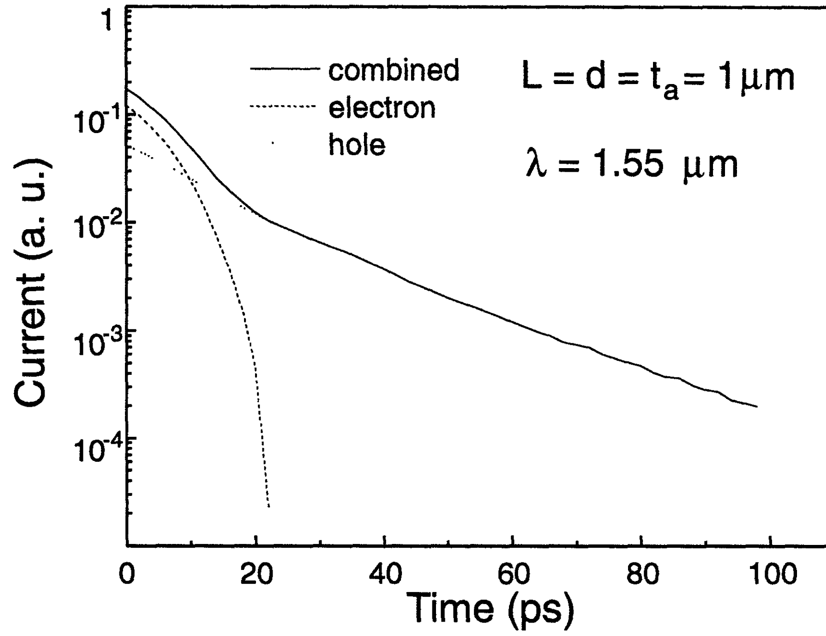

(a)

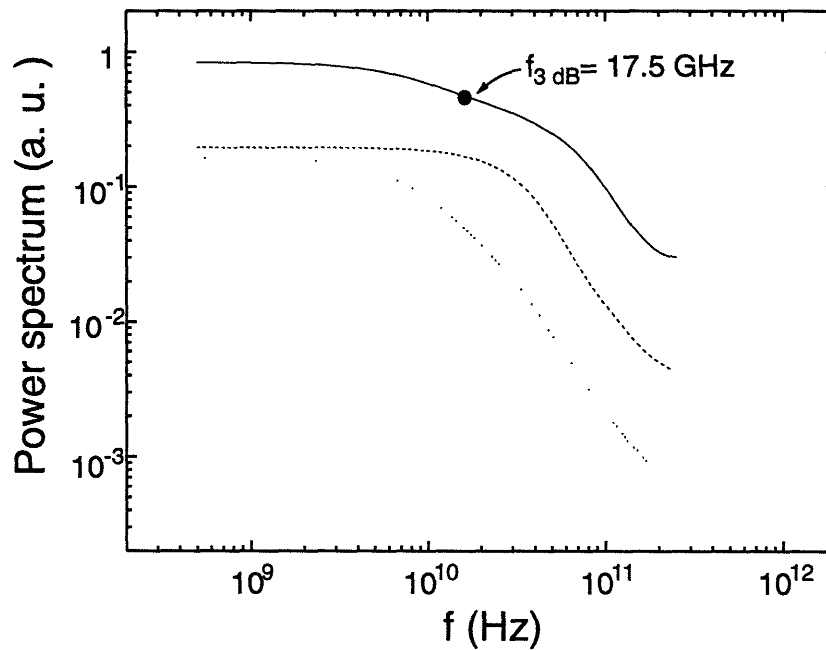

(b)

Figure 3-4: (a) Temporal response of a photodetector with L = d = 1 μm, at V = 10 volts, with the electron and hole contributions shown separately, and (b) the corresponding power spectra.

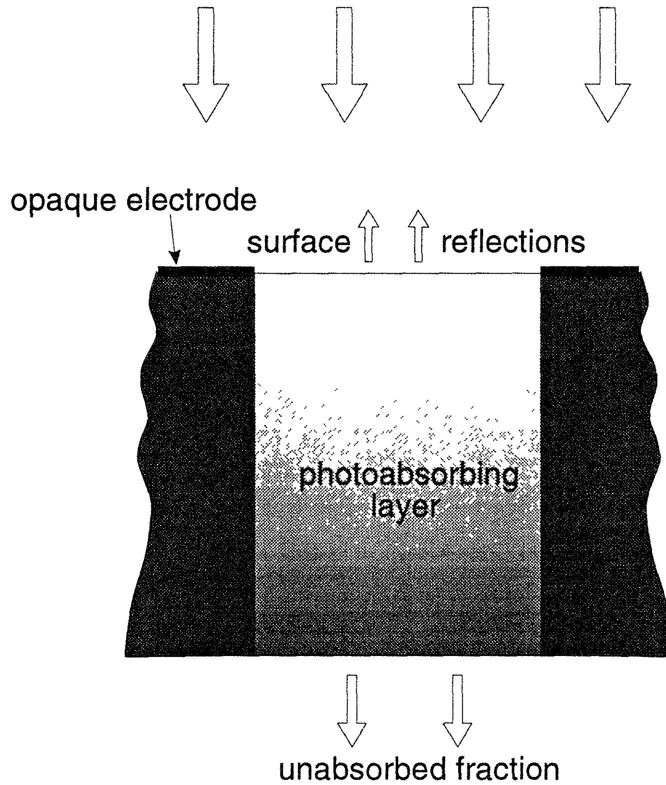

Figure 3-5: Schematic representation of the effects that limit the external quantum efficiency of an MSM photodetector.

3.3 Quantum efficiency of MSM structures

The internal efficiency, η_{int}, of an MSM photodetector is defined as the number of electron-hole pairs collected per photon absorbed within the active layer. By applying a sufficiently large bias to the detector fingers, it is typically possible to extract almost all the carriers generated within the photoabsorbing layer. As a result, η_{int} is generally very close to unity. The external quantum efficiency, η_{ext}, of the device on the other hand measures the number of electron-hole pairs collected for each *incident* photon [1]. With $\eta_{int} \simeq 1$, η_{ext} is given by:

$$\eta_{ext} = \frac{total\ intensity\ absorbed}{total\ incident\ intensity} \tag{3.29}$$

Fig. 3-5 shows the schematic cross-section of a top-illuminated MSM photodetector. The total intensity absorbed by the photoactive semiconductor layer is limited

by the following factors:

- Shadowing effect of the opaque metal fingers. Hence, only a fraction L/(L+d) of the incident intensity falls on an open or effectively "useful" region of the device.

- A fraction, R, of the light incident within the interelectrode spacing is lost due to reflections at the air-semiconductor boundary. This effect contributes a scaling factor of (1-R).

- With a finite active layer thickness, t_a, only $(1 - e^{-t_a/L_\lambda})$ of the transmitted intensity gets absorbed within the semiconductor layer. Assuming that there are no back reflections, the remainder of it exits through the bottom interface.

In practice, MSM photodetectors are covered with an anti-reflection coating which limits the losses due to reflections at the air-semiconductor interface. If such a coating suppresses the reflections completely (i.e. R = 0),

$$\eta_{ext} = \frac{L}{L+d}\left(1 - e^{-t_a/L_\lambda}\right) \tag{3.30}$$

3.4 Design tradeoffs for MSM photodetectors

The results of the preceding sections were used to examine the tradeoffs involved in scaling $In_{0.53}Ga_{0.47}As$ MSM photodetectors on InP. In particular, we evaluated the effect of varying the finger spacing and the thickness of the active layer on both the power bandwidth and the quantum efficiency of the device.

Fig. 3-6 shows the f_{3dB} and η_{ext} plots for L = d = 1 μm at V = 10 volts, and t_a = 1, 2 and 3 μm. The upper and lower bounds on f_{3dB}, for a given t_a, correspond to v_{max} and v_{min} respectively. The observed trends are easy to explain. As the thickness of the active layer is increased, a larger fraction of the incident light is absorbed by the semiconductor and η_{ext} improves. The deleterious effect of increasing t_a, however, is that carriers are generated further away from the collecting electrodes, in regions with

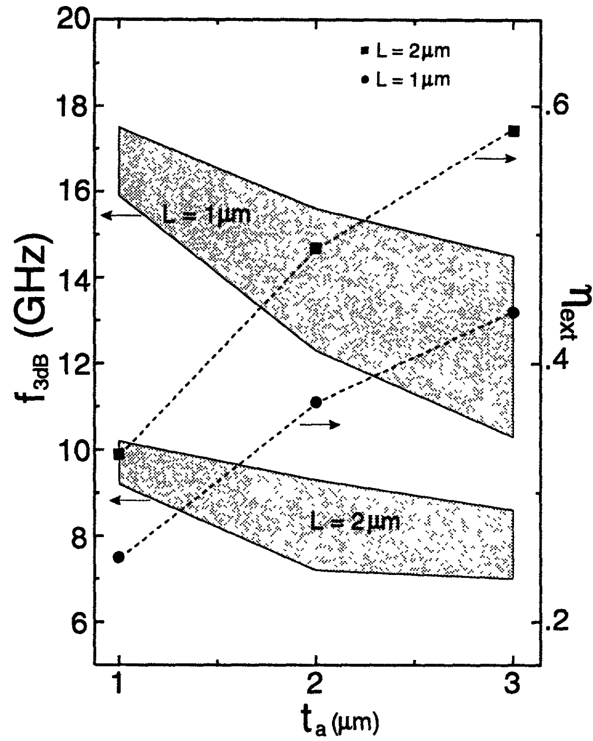

Figure 3-6: The f_{3dB} and η_{ext} plots for L = d = 1 μm, and L = 2d = 2 μm at V = 10 volts. In each case, the active layer thickness, t_a, was assumed to be 1, 2 and 3 μm.

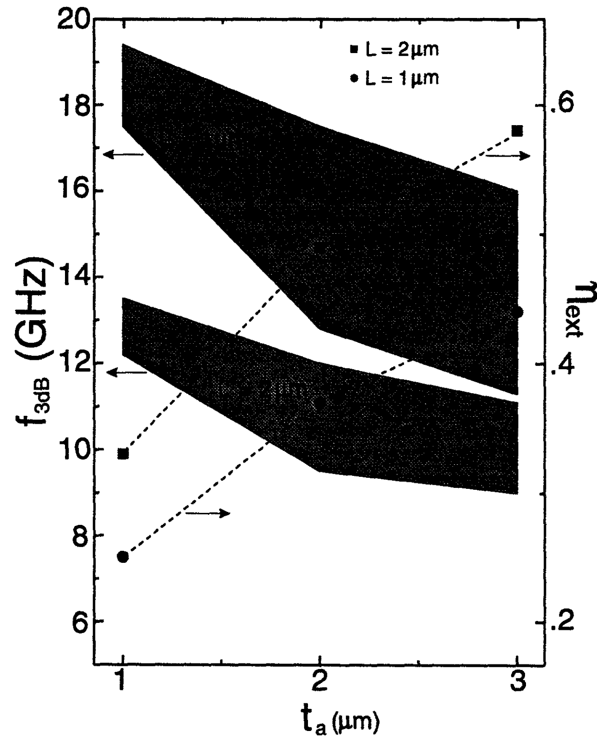

Figure 3-7: A parallel analysis of the f_{3dB} and η_{ext} tradeoff using the far-field approximation of Gvozdić et al.'s expression. Exaggerated 3 dB power bandwidths illustrate the importance of the Fermi-level pinning boundary condition.

reduced electric fields. They therefore take a longer time to reach the detector fingers. This leads to a temporal response with a more pronounced tail and a subsequent reduction in the power bandwidth of the device.

To explore the effect of scaling the finger spacing, the above exercise was repeated for L = 2d = 2 μm, with V = 10 volts. The results are summarized in Fig. 3-6. For this geometry, an extra 16% of the unit cell is open to the incident light. Hence, η_{ext} for each value of t_a is proportionately higher than the previous case. The bandwidth of the detector, however, gets severely compromised on adopting this new design. As pointed out earlier, enlarging the unit cell not only increases the net distance covered by the photogenerated carriers, but also scales down the field throughout the structure. This results in longer transit times and a reduced f_{3dB}.

The f_{3dB} and η_{ext} tradeoff was also examined using the far-field approximation of Gvozdić et al.'s expression [25]. The basic trends observed in this case, Fig. 3-7, were the same as those noted earlier. The 3 dB power bandwidth for each detector geometry, however, was found to be larger than the corresponding value shown in Fig. 3-6. For L = d = 1 μm, for example, f_{3dB} was about 10% higher, while for L = 2d = 2 μm the discrepancy was nearly 30% on average. The observed difference results from the fact that Gvozdić et al.'s treatment overestimates the field in MSM structures with Fermi level pinning. This translates to reduced transit times, and exaggerated bandwidths. The extent of this overestimation varies from one geometry to the other, and directly follows F(L/d). Hence, the difference in f_{3dB} worsens as L/d is increased.

Photodetector designs with L/d > 1 are common since they yield high-responsivity devices. Our analysis above shows that ignoring the Fermi level pinning condition in these cases results in over optimistic estimates of f_{3dB}. When settling for a compromise between η_{ext} and f_{3dB}, such oversight can lead to design choices in which the eventual price paid in terms of a reduced bandwidth may be far more severe than expected. Given its importance, we decided to explore this issue in greater detail.

3.5 Impact of Fermi level pinning on f_{3dB}

In order to understand the impact of this boundary condition on the 3 dB bandwidth, a variety a detector geometries were considered in more detail. Starting with a prototype design in which L, d, and t_a were all set at 1 μm, each dimension was alternately halved and doubled. Typical designs evaluated under this scheme were: L = d = 1 μm, t_a = 2 μm; L = t_a = 1 μm, d = 0.5 μm etc. For each such setting, the 3 dB bandwidth was calculated in the same manner as described in the preceding sections, for cases both with and without Fermi level pinning. The one exception in this case, however, was that f_{3dB} was computed only for $v_{e,sat} = 1 \times 10^7$ cm/s. Since we were simply interested in observing the general effect of incorporating Fermi level pinning, the choice $v_{e,sat}$ was not critical for our analysis.

The results of these calculations are summarized in Fig. 3-8. As can be seen, when t_a was varied from 2 μm to 0.5 μm, f_{3dB} was found to increase monotonically. In this case, ignoring the Fermi level pinning condition caused the bandwidth to be overestimated by nearly 10% (t_a = 0.5 μm was an exception). With the L/d ratio fixed at 1, based on our analysis in Chapter 2 we would expect this discrepancy to be roughly constant for each setting of t_a. The fact that the results for t_a = 0.5 μm did not conform to these expectations, however, was not surprising. With such a thin active layer, nearly all carriers within the unit cell are under velocity saturation when the applied bias is 10 Volts. As a result, the discrepancy in the field distributions, as predicted by F(L/d) (see section 2.4), does not translate one for one to the f_{3dB} value.

The 3 dB bandwidth also increased steadily when L was reduced. This trend results from a stronger electric field and a reduced path length for the carriers; the two positive effects of decreasing the finger spacing. A third, though detrimental, effect of reducing L is that the field decays much faster with the distance from the surface [1]. For the set of designs that were considered, however, this effect was clearly not the dominant one. Furthermore, as before, on ignoring Fermi level pinning we

[1] The characteristic decay length is $(L+d)/\pi$.

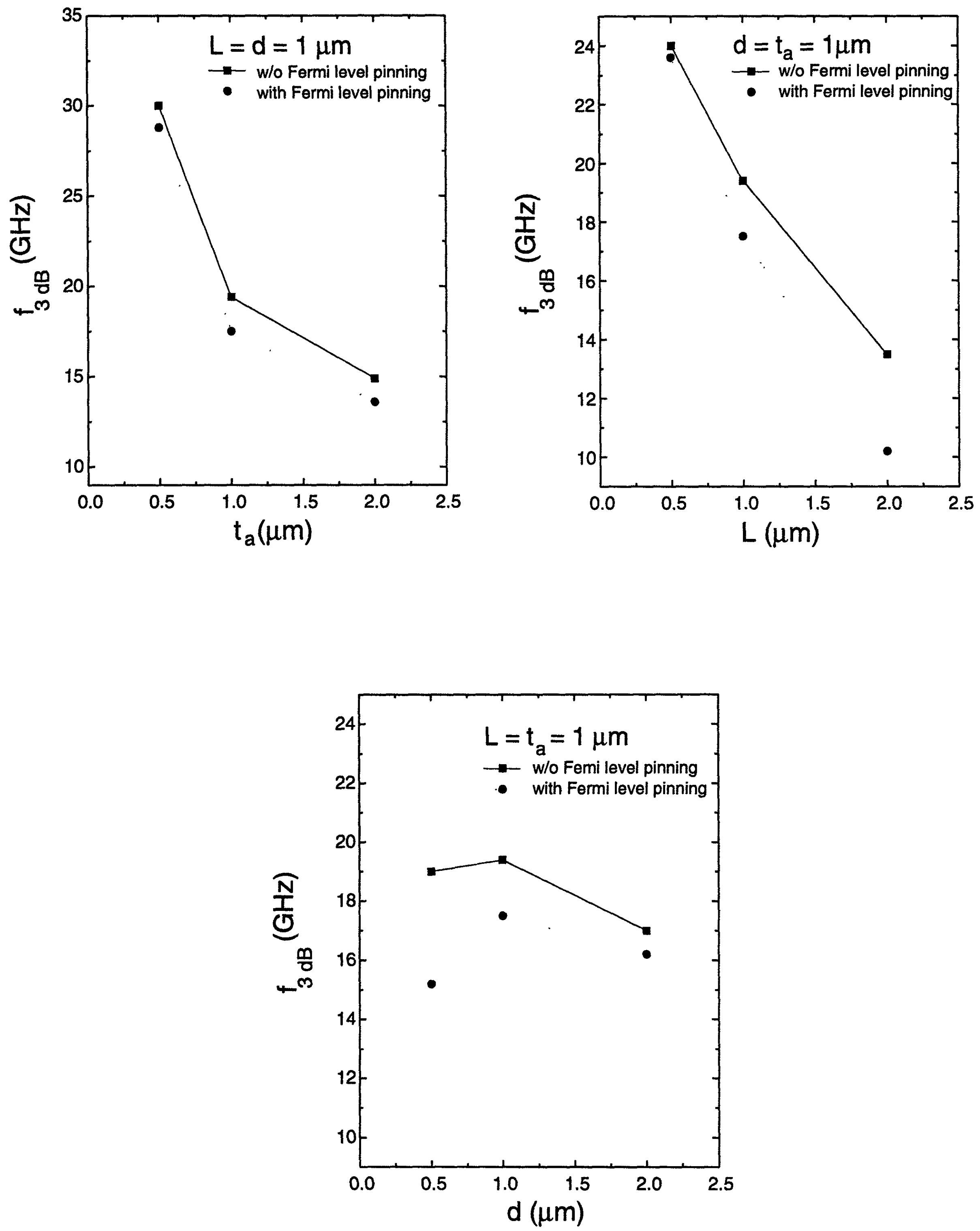

Figure 3-8: Results highlighting the impact of Fermi level pinning.

obtained exaggerated estimates for f_{3dB}. As expected, the discrepancy worsened when the L/d ratio was increased.

Interesting results were obtained on varying d. As the finger width was reduced from 2 μm to 0.5 μm, f_{3dB} was found to first increase and then fall off. These trends can again be explained as an interplay of the three effects outlined above. Here, however, the effect of a more rapidly decaying field happened to override the other factors comparatively easily, causing f_{3dB} to drop when d was halved from 1 μm to 0.5 μm. More importantly, the drop in the bandwidth was more pronounced when Fermi level pinning was accounted for. This clearly emphasizes the need for incorporating the correct boundary condition in analyses that lead to the final design choices.

3.6 Summary

Using the results of the previous chapter, we have developed an explicit expression for the transit time of carriers generated within the active layer of an MSM photodetector. This in turn has been utilized in evaluating the effect of scaling critical device dimensions on the detector bandwidth and quantum efficiency. By computing the 3 dB bandwidth for a variety of designs, both with and without Fermi level pinning, we have also successfully highlighted the importance of this boundary condition. The results of our analysis underscore the need to account for Fermi level pinning in order to establish correct design criteria for MSM photodetectors.

Chapter 4

Technology for InAlAs/InGaAs MSM photodetectors

4.1 Overview

This chapter focuses on the device design and process technology issues associated with InAlAs/InGaAs MSM photodetectors. We report a fabrication sequence that successfully incorporates X-ray lithography in the standard MSM photodetector process to yield devices with sub-micron size fingers and spacings. This is followed by a description of the setup used to perform a DC characterization of the detectors. The results of these measurements are discussed last.

4.2 Device design

Fig. 4-1 shows the schematic cross-section of our target InGaAs MSM photodetector. Work done in the past on these devices has shown this particular combination of layers to be the one that optimizes the operation of the detectors at long wavelengths. The 1 μm thick InGaAs layer is the main region where the incident intensity is absorbed. The barrier enhancement layer (500 Å InAlAs), positioned directly below the metal fingers, in turn serves to increase the Schottky height of the contact. Since an MSM detector essentially consists of two back-to-back Schottky diodes, its

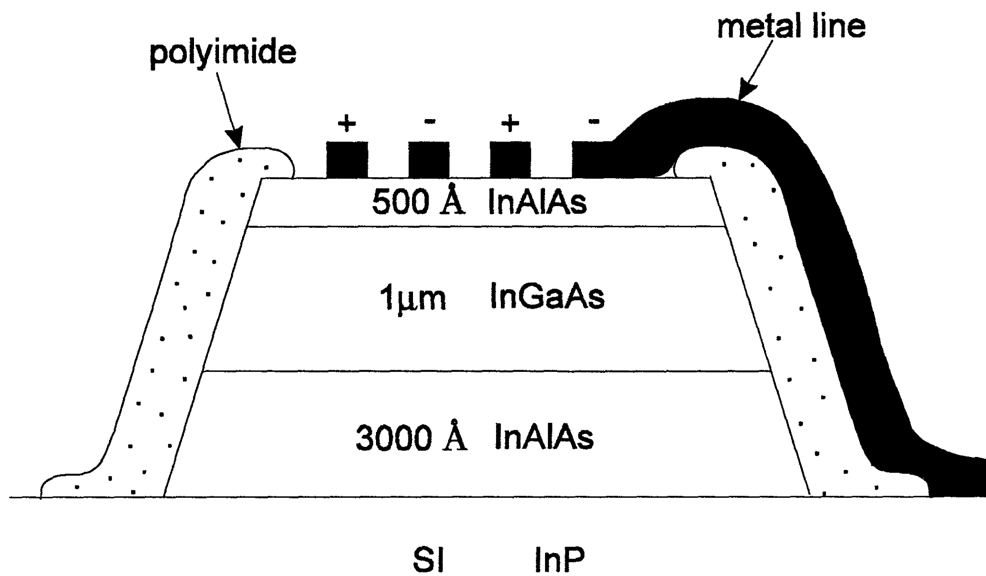

Figure 4-1: Schematic cross-section of the target MSM photodetector.

performance depends critically on the quality of these contacts. For GaAs-based detectors an acceptable Schottky barrier height can generally be achieved by directly metallizing the active layer. InGaAs MSM photodetectors, on the other hand, suffer from excessive leakage currents when the contacts are formed directly on the semiconductor. This drawback, which is attributed to the low Schottky barrier height (about 0.2 eV) of the metal-InGaAs system [32], [33], has precluded the successful operation of InGaAs-based photodetectors. In order to fully exploit the potential of InGaAs-based MSM photodiodes, recent studies have focused on overcoming this problem. Devices with high bandgap epitaxial layers inserted between the metal contacts and the photoactive layer have been under investigation. Researchers have experimented with materials both lattice-matched [34]-[36] and lattice-mismatched [18], [37] to the underlying InGaAs layer. Encouraging results have been achieved with a lattice-matched InAlAs layer. Detectors with an arrangement of layers similar to that shown in Fig. 4-1, for example, have been reported to have dark currents between 1-10 pA/μm^2 [11], [20].

The 3000 $\AA$ InAlAs buffer layer, that lies between the active InGaAs and semiin-

sulating InP layers, is the most recent addition to the MSM structure. Its presence has been shown to reduce the parasitic capacitance of the device over the 100 MHz - 1 GHz range; hence improving the RC-limited bandwidth of the detector substantially [38].

The polyimide ring, shown only partially in the figure, runs around the entire perimeter of the mesa. It eliminates a potential leakage path by preventing the metal lines from contacting the active layer along the side-wall. In addition to this, it is also known to aid the continuity of these lines over the mesa edges [39].

In most practical designs, the transit time of the photogenerated carriers proves to be the bottleneck for the detector bandwidth. As shown in the previous chapter, this limitation can be overcome by scaling down critical device dimensions, such as the finger width and the interelectrode spacing. In the past, the use of standard photolithographic techniques has yielded detectors with finger widths of about 0.5 μm. Reduction of the minimum feature size beyond this limit can be achieved by patterning the fingers with advanced lithographic processes. We decided to use X-ray nanolithography to this end. By employing this technology, we also hoped to benefit from some of its other outstanding attributes. Its broad process latitude, for example, is conducive for higher yield. From a long term perspective, the large depth-of-focus offered by this technology could potentially be used to simultaneously fabricate sub-micron size gates for FETs, positioned adjacent to the detectors, even if they are located at a substantially different height. The subsequent integration of these components would be an important step towards realizing high bandwidth, monolithically integrated receivers.

4.3 Brief fabrication sequence

Fig. 4-2 shows a flow diagram of the process sequence used to fabricate the devices. To begin with, the wafers were solvent cleaned and the surface oxide was removed with a subsequent dip in Semico. Mesa isolation was then achieved by etching the samples in H_2SO_4:H_2O_2:H_2O (1:10:110) which removes InAlAs and InGaAs at rates of

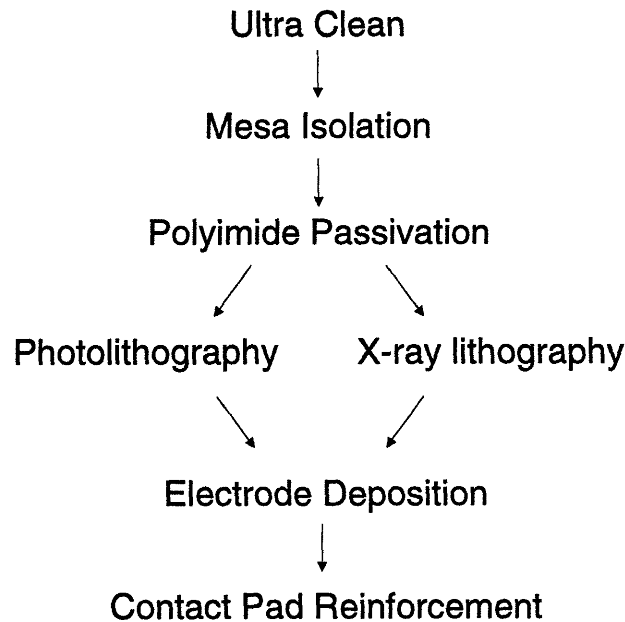

Figure 4-2: The process flow.

3500 Å/min and 2500 Å/min, respectively. The photosensitive polyimide (Probimide 408) ring was patterned around the mesa edges next, and then cured at 160°C for 2 hours.

At the completion of this step, the samples were cleaved in half. Conventional photolithography was then used to pattern the metal fingers on one set of wafers. An image reversal process was utilized to achieve the negative resist profile required for good lift-off. This was followed by a Ti/Au (200 Å/700 Å) evaporation, and subsequent lift-off in acetone. The contact pads were reinforced with an additional 2500 Å of Au. Detectors with 1 μm wide fingers and spacings were achieved as a result (see Fig 4-3).

X-ray lithography was used, on the other hand, to define the electrode fingers on the second set of wafers. The mother mask for this process step was patterned by e-beam lithography at the Naval Research Laboratories. The corresponding daughter mask, used to transfer device patterns onto the wafers, was prepared by Martin Burkhardt at the Nanostructures Laboratory at MIT. The devices were fabricated by spinning a layer of PMMA (950K, 4%) on the wafers, exposing it for 8 hours at a dose

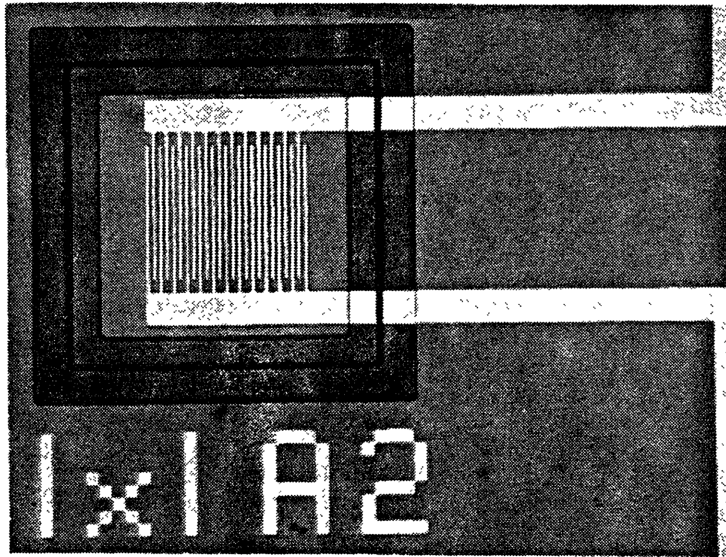

Figure 4-3: An InAlAs/InGaAs/InP MSM photodetector with 1 μm wide fingers and spacings, that was fabricated at TRL, MIT.

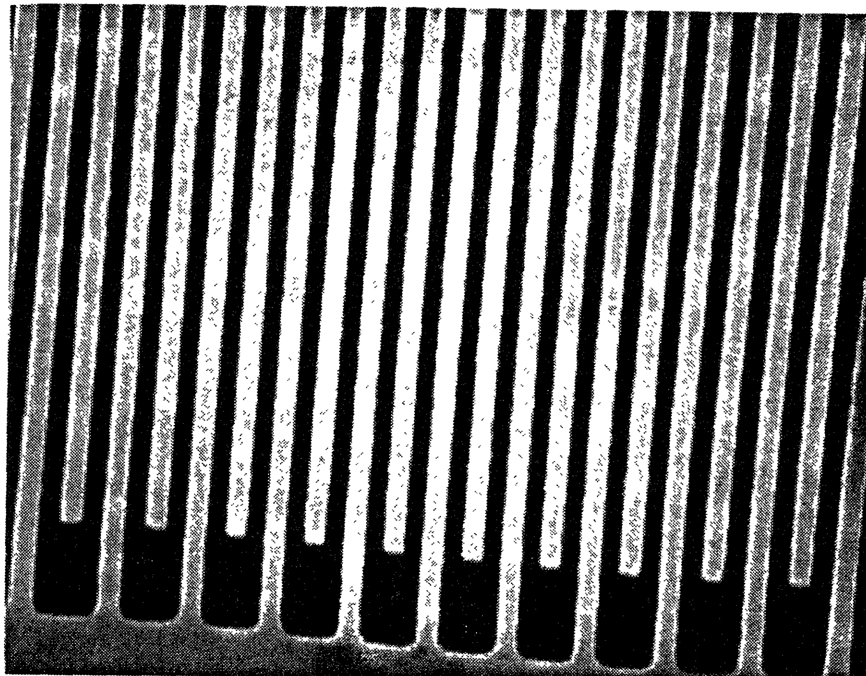

Figure 4-4: SEM micrograph of an MSM photodetector with 0.3 μm wide fingers and spacings. The detector fingers were patterned with X-ray lithography.

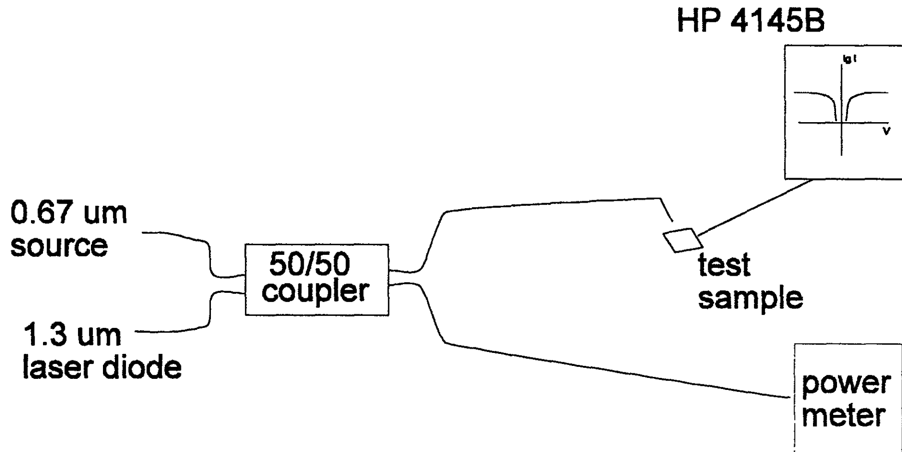

Figure 4-5: Schematic view of the experimental setup designed to characterize the MSM detectors.

of approximately 1 KJ/cm^3, and then developing in MIBK:IPA (4:6) solution for a minute. Following this, the fingers were formed by depositing Pt/Ti/Au (200 Å/200 Å/1600 Å), and performing lift-off in acetone. The contact pads were subsequently reinforced with Au. Finger widths and spacings of 0.3 μm were realized successfully with this combination of process parameters (see Fig. 4-4).

4.4 Measurement setup

The setup used to perform DC measurements on these detectors is shown schematically in Fig. 4-5. The 0.67 μm visible source was used first to position the SMF-28 fiber tip directly above the active area of the device. Switching over to the infra red laser (1.3 μm, 2.5 mW CW), the I-V characteristics of the detectors were then determined with an HP 4145B Semiconductor Parameter Analyzer for a series of incident power levels. The use of the 3 dB coupler enabled us to monitor these power levels simultaneously on a digital meter.

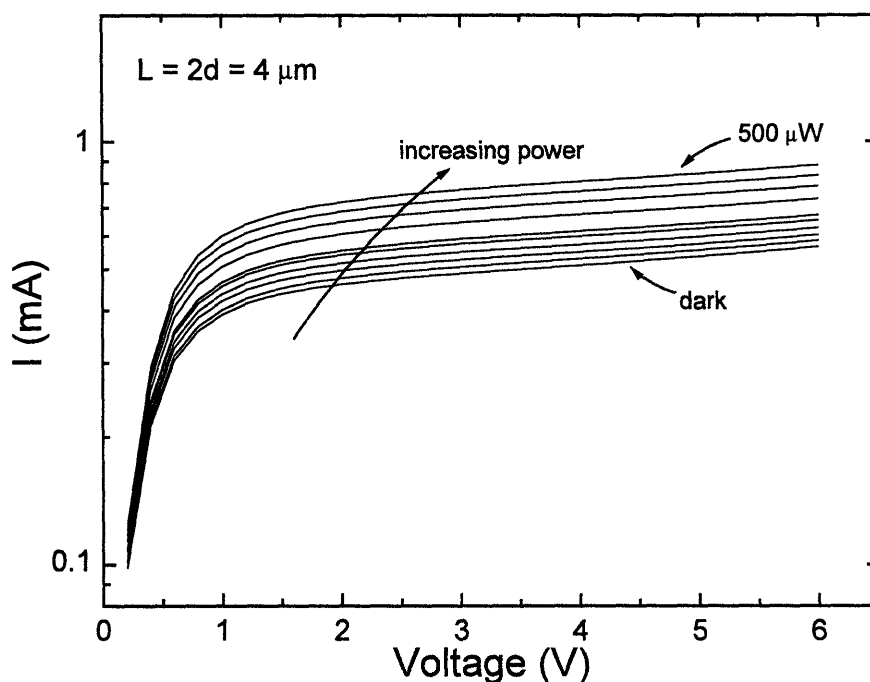

Figure 4-6: Typical I-V characteristics of an MSM photodetector.

4.5 Results and discussion

The characterization scheme described above was tested on InAlAs/InGaAs/InP MSM photodetectors that had been fabricated previously by Peter Nuytkens at MIT. The results of these measurements are shown in Fig. 4-6. Even though the dark current in these detectors was found to be unusually high ($\sim$ 0.5 mA at V = 5 Volts), the device characteristics in general were reasonable. For each power setting, the detector current flattened out beyond a certain applied voltage. This knee in the I-V characteristics corresponds to the minimum field required to sweep out the majority of photocarriers generated within the active InGaAs layer.

Similar measurements made on devices that we had patterned with conventional photolithography yielded anomalous results. The detectors appeared almost insensitive to the 1.3 μm laser light when probed electrically at the contact pads. On systematically analyzing a variety of detector designs, we concluded that the metal lines in these devices suffered from poor step coverage along the mesa slopes. In retrospect, we feel that a thicker layer of metal (3000 $\AA$ as opposed to only 900 $\AA$) should

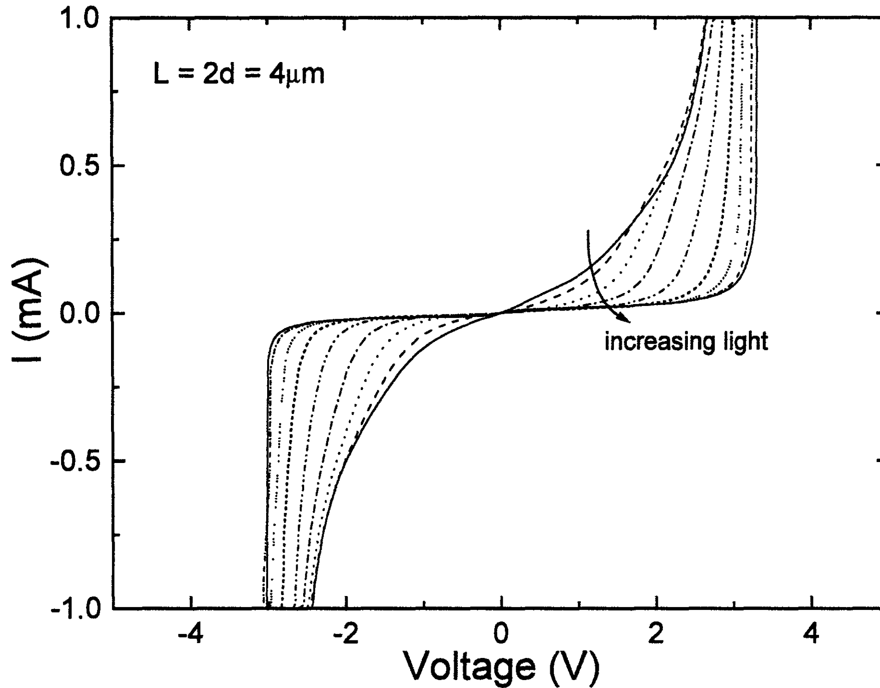

Figure 4-7: Anomalous I-V characteristics exhibited by the fabricated devices.

have been used to form the lines and fingers. In order to engage the active areas of these detectors, we contacted the metal lines on the mesas directly. Fig. 4-7 shows the results of these measurements. As compared to the typical I-V characteristics shown in Fig. 4-6, this set of devices showed a sudden surge in the diode current at very low voltages. Furthermore, the breakdown voltage consistently shifted out to higher values as the incident intensity was increased. We observed similar results on probing the detectors that were patterned with X-ray lithography.

Although we were unable to identify a convincing reason for the abnormal behavior of the devices, we narrowed down the possibilities. Since switching from Ti/Au to Pt/Ti/Au for the electrode metal did not affect the detector characteristics, we concluded that the choice of metal was not the cause of the problem.

The presence of deep level traps is yet another phenomenon that has been shown to produce anomalous characteristics (similar to those shown in Fig. 4-7) in β-$FeSi_2$-n-type Si diodes [40]. As explained by the author, the traps get populated when radiation impinges on the active layer. They then modulate the width of the existing

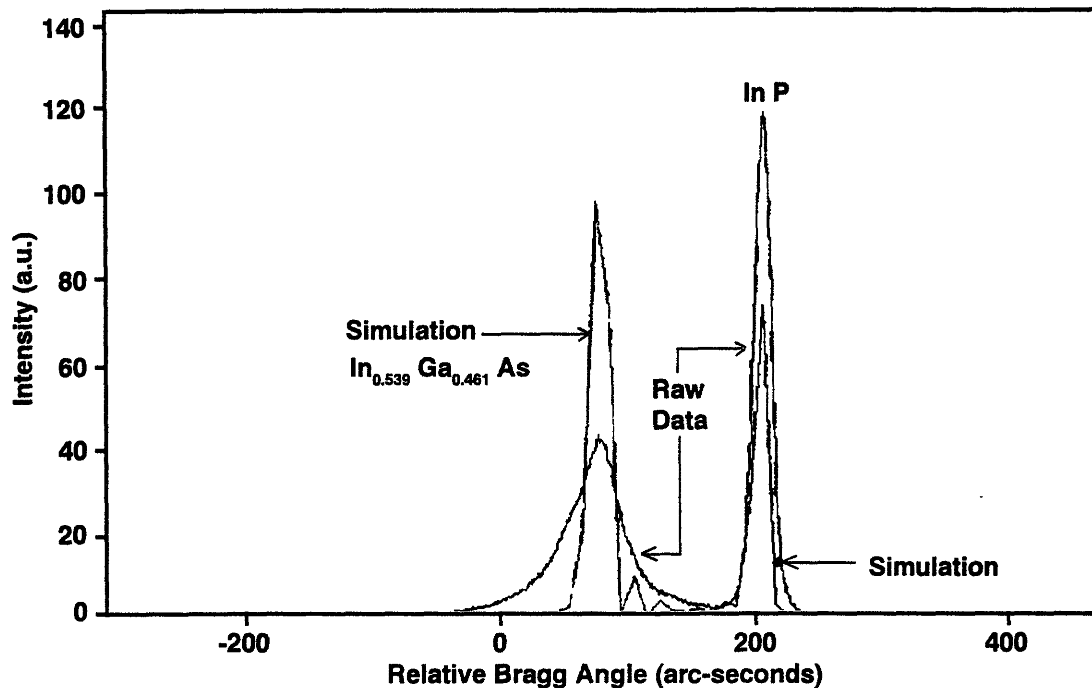

Figure 4-8: DCXRD data for the heterostructure.

depletion region, causing it to shrink in size as the incident intensity is increased.

In the case of an MSM photodetector this would imply that, for a fixed bias, as the light intensity is increased, both the number of carriers collected at the electrodes and the field strength within the structure would be reduced. Both these effects are evident in the characteristics shown in Fig. 4-7. As can be seen, on increasing the light intensity a lower current was recorded at the fingers for the same applied bias. In addition to this, the breakdown voltage also shifted out to higher values, reflecting that the effective field within the device had been reduced.

To explore this possibility further, we inspected the double-crystal X-ray diffraction (DCXRD) rocking curve for the unprocessed heterostructure. As shown in Fig. 4-8, the FWHM of the peaks in the x-ray data were broader than nominally expected. Based on these results, we feel that the questionable quality of the starting material might have induced the trap-related phenomenon in our devices also.

4.6 Summary

We have developed and implemented the technology for fabricating sub-micron size MSM photodetectors. Our efforts have yielded devices with 0.3 μm wide fingers and spacings. The detectors, however, were found to have anomalous I-V characteristics. We suspect that the poor quality of the starting material is responsible for this abnormal behavior.

Chapter 5

Conclusion

The importance of InGaAs/InP MSM photodetectors in long-haul optical communication systems cannot be overemphasized. A number of research projects, in the past, have been directed towards designing these devices for high speed and high sensitivity performance. Our work underlines the need to model the physics of these structures accurately in order for such efforts to materialize.

In particular, we have found that it is important to take into account the Fermi level pinning boundary condition, at the top exposed surface, when modeling the field distribution in III-V semiconductor-based MSM photodetectors. Failure to do so leads to exaggerated estimates of the electric field within these structures. The extent of this overestimation grows with the interelectrode spacing/finger width (L/d) ratio, as the surface begins to play an increasingly important role in determining the field strength.

The spill-over effect of incorrectly modeling the field distribution results in over optimistic estimates of the detector bandwidth. For $L/d = 2$, for example, the 3 dB bandwidth is overestimated by nearly 30% if the Fermi level pinning condition is ignored. Since a strong tradeoff exists between the quantum efficiency and the 3 dB bandwidth of MSM photodetectors, such oversight can prove detrimental for efforts aimed at optimizing the operation of these devices.

In addition to this, we have implemented a four-step process sequence for fabricating InAlAs/InGaAs/InP MSM photodetectors. In order to realize high speed

devices, X-ray nanolithography was used to scale down the detector fingers and spacings. We managed to achieve a minimum feature size of 0.3 μm, and in the process established the compatibility of this technology with the standard steps used to fabricate MSM detectors. We have by no means exploited the full potential of this lithographic technique. Future efforts should be directed towards scaling the critical detector dimensions even further.

Appendix A

Potential distribution in III-V semiconductor based MSM photodetectors

The potential distribution in an MSM structure with Fermi level pinning at the semiconductor surface is given by :

$$\Phi(z) = \frac{V}{\pi} Re \left[sin^{-1} \frac{\sqrt{1 - sin^2 \frac{\pi L}{2(L+d)}}}{\sqrt{sin^2 \frac{\pi z}{L+d} - sin^2 \frac{\pi L}{2(L+d)}}} \right] \tag{A.1}$$

where $z = x + iy$.

To show that (A.1) above satisfies the boundary conditions shown in Fig. A-1, let us make the following substitution:

$$sinC = \frac{\sqrt{1 - sin^2 \frac{\pi L}{2(L+d)}}}{\sqrt{sin^2 \frac{\pi z}{L+d} - sin^2 \frac{\pi L}{2(L+d)}}} \tag{A.2}$$

Using this simplification, (A.1) can be rewritten as:

$$\Phi(z) = \frac{V}{\pi} Re\,[C] \tag{A.3}$$

In the most general case, $C = a + ib$ where both a and b are real numbers. Conse-

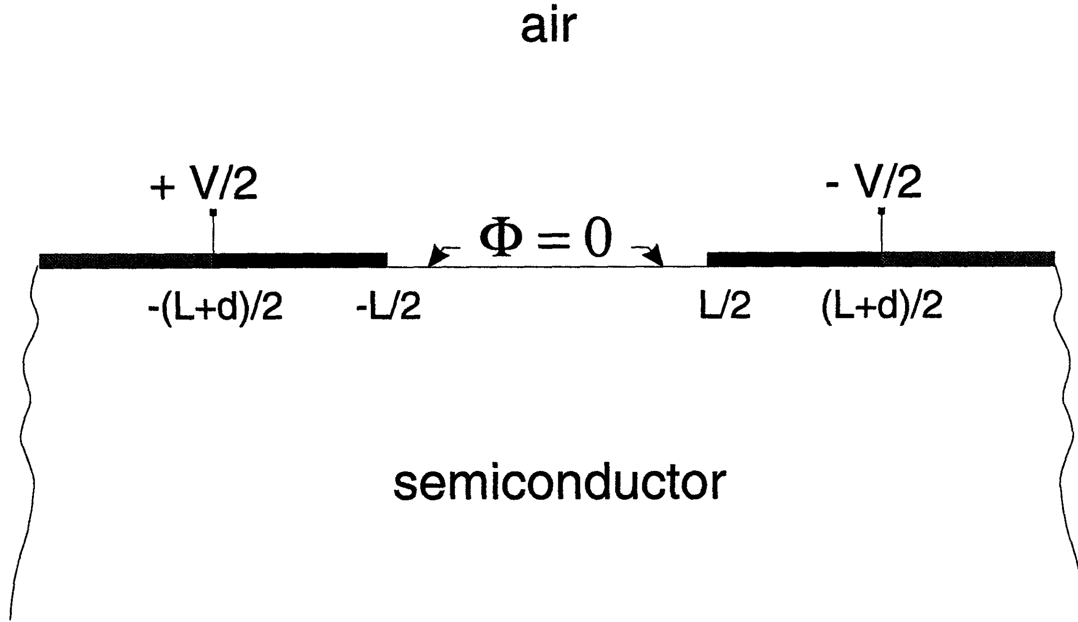

Figure A-1: Boundary conditions along y = 0

quently,

$$\sin C = \sin(a + ib) = \frac{1}{2}\sin a(e^b + e^{-b}) + \frac{i}{2}\cos a(e^b - e^{-b}) \tag{A.4}$$

With $y = 0$, the interelectrode spacing is demarcated by the limits -L/2 $< x <$ L/2. For this range of values $\sin C$ is purely imaginary. It follows from (A.4) then that,

$$\frac{1}{2}\sin a(e^b + e^{-b}) = 0 \tag{A.5}$$

The equation above is satisfied when a = 0. Subsequently, (A.3) reduces to:

$$\Phi(|x| < L/2, y = 0) = \frac{V}{\pi}Re\,[ib] = 0 \qquad\qquad QED$$

In the case of the metal electrodes, L/2 $< |x| <$ (L+d)/2. From (A.2) we can conclude that $\sin C$ is real over this range. Hence,

$$\frac{1}{2}\cos a(e^{b}-e^{-b})=0 \tag{A.6}$$

Furthermore, (A.2) also requires that $\sin C$ lie in the interval $[1, \infty]$. These two conditions are simultaneously satisfied if $a = \pm\ \pi/2$, with no restrictions on b. In this case, therefore, (A.3), simplifies to:

$$\Phi(L/2<|x|<(L+d)/2, y=0)=\frac{V}{\pi}Re\left[\pm V/2+ib\right]=\pm V/2 \qquad QED$$

Appendix B

2D Poisson simulations

The 2D Poisson simulator used in our work utilizes the method of finite differences to compute a variety of parameters (including the electric field distribution) for a specified semiconductor structure [29]. The boundary conditions that the program is designed to handle, however, do not include the $\mathcal{E}_x(z) = 0$ condition that prevails along the vertical edges of the unit cell ($|x| = \mathrm{L}/2$) defined in Chapter 2. This problem can be circumvented by simulating a structure that is twice the size of the original cell. On making this simple modification, we find that $\Phi = 0$ along the vertical edges of the enlarged cell. This boundary condition can be conveniently handled by the simulator.

Fig. B-1 shows the details of the structure that was used to simulate the L = d = 0.1 μm case with V = 10 volts. Here, unlike Chapter 2, the origin of the coordinate system corresponds to the upper left corner of the simulated structure. It is important to keep this in mind when comparing the results of these simulations with those predicted by the analytical expression derived in Chapter 2. The input file for the structure shown in Fig. B-1 is given below:

start regions
GaAs 0 0 4000 20000 Ndd = 0 Nda = 0
stop regions

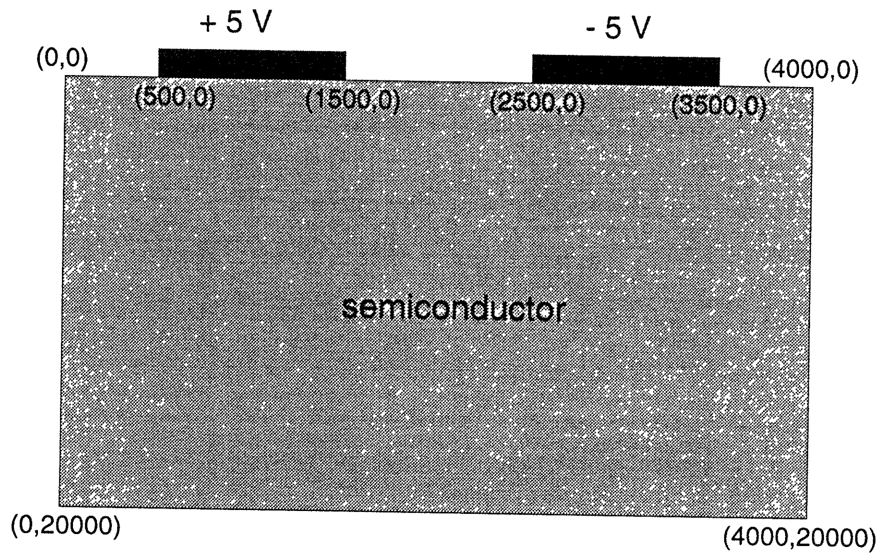

Figure B-1: Simulated structure.

temp = 300

fullyionized

no holes

no elec

bc 0 0 500 0 schottky = 0.0 v1

bc 500 0 1500 0 schottky = 0.0 v2

bc 1500 0 2500 0 schottky = 0.0 v3

bc 2500 0 3500 0 schottky = 0.0 v4

bc 3500 0 4000 0 schottky = 0.0 v5

bc 0 0 0 20000 schottky = 0.0 v6

bc 4000 0 4000 20000 schottky = 0.0 v7

bc 0 20000 400 20000 schottky = 0.0 v8

dy = 200

dx = 50

v1 0.0

v2 5.0

v3 0.0

v4 -5.0

v5 0.0

v6 0.0

v7 0.0

v8 0.0

Setting the thickness of the active layer to 2 μm achieves the effect of a semi-infinite photoabsorbing region. The "no elec" and "no holes" statements in the program listing guarantees that free carriers are ignored during the simulation. These features together therefore ensure that the situation being simulated is consistent with the one solved by the method of conformal mappings in Chapter 2.

To compare the results obtained from the simulation outlined above with those given by the analytical expression derived earlier, we only need the field distribution in the region demarcated by $1000 < x < 3000$ (see Fig. B-1 for context). These values can be easily obtained from the resulting output file.

Appendix C

InGaAs/InP MSM Photodiode Process Sequence

1. Equipment/Materials Preparation and Misc. Notes:

   (a) Perform cleaning procedures on all tools and "glassware":
   Minimum "glassware":

      i. 7 glass 600 ml beakers - 2 acid, 2 solvent, 2 deionized H_2O, and 1 photoresist developer.
      ii. 1 glass or poly (poly preferred) 100 ml graduated cylinder.
      iii. enough petri dishes and covers to hold samples.

   (b) Make sure the following chemicals are in stock:

      i. solvents: TCA, acetone, and methanol
      ii. acids/bases: H_2SO_4, H_2O_2, Semico clean
      iii. photolithography: KTI 820-27cSt resist, HMDS adhesion promoter, OCG 934 1:1 developer, QZ 3289 promoter, QZ 3290 solvent, Probimide 408, QZ 3301 developer, QZ 3312 rinse, KTI PMMA 950K 4% resist, MIBK developer, IPA, AZ 5214-E resist, AZ 422-MIF developer

   (c) For best results, prepare the following "etchant #1" concentrate in advance:
   H_2SO_4:H_2O_2:H_2O 1:10:10 (20 ml : 200 ml : 200 ml)
   Note: allow concentrate to cool down before using. Solution lasts for about 3 weeks.

   (d) Always read at least one procedure ahead of your present place in the process and schedule the required equipment in advance to avoid unnecessary delays.

2. Mesa Isolation:

   (a) Ultra clean:

i. TCA: warm 60-70°C, 2 min., twice.
ii. acetone, ultrasound, 2 min., twice.
iii. methanol, 1 min.
iv. deionized H_2O rinse, 1 min., and N_2 blow dry. Store in dry box if not processing immediately.

(b) Photolithography:

i. preparation:
   A. check that pre-bake oven is on, and set to 90°C.
   B. check that post-bake oven is on, and set to 120°C.
   C. spray mask MESA with acetone/methanol, rinse with deionized H_2O, and N_2 blow dry to clean.
ii. Semico clean, ultrasound, 1 min.
iii. deionized H_2O rinse, 1 min., and N_2 blow dry.
iv. spin promoter, HMDS, 4000 rpm, 30 sec.
v. spin resist, KTI 820-27cSt, 4000 rpm, 30 sec. (nominal thickness: 1.3 μm).
vi. heat in pre-bake oven, 90°C, 30 min.
vii. cool down 5 min.
viii. test expose dummy samples, mask MESA (Estimate: 2.5 sec on ST, SOFT CONT).
ix. develop in OCG 934 1:1, 1 min.
x. deionized H_2O rinse, 1 min., twice, and N_2 blow dry.
xi. microscope inspection.

Previous data on p. _______ Power = _______ W
Intensity = _______ mW/cm^2

Sample ID #						
exp. time						
over/under						
alignment						
comments						

xii. expose, develop, and inspect device samples.

Previous data on p. _______ Power = _______ W
Intensity = _______ mW/cm^2

Sample ID #						
exp. time						
over/under						
alignment						
comments						

xiii. heat in post-bake oven, 120°C, 30 min.

(c) Mesa Etch:

i. prepare mesa etchant (mix very well, using magnetic stirrer):
1 part concentrate to 10 parts H_2O (20 ml : 200 ml), *or*, *if concentrate is not available*, H_2SO_4:H_2O_2:H_2O 1:10:220.
Note: if preparing fresh etchant, make sure etchant cools down to room temperature prior to use.

ii. descum in asher to etch 200Å of resist:
Power = 200 W, Time = 2 $min.$
Loading =_____, Tuning =_____

iii. Semico clean:

- deionized H_2O rinse, 1 min.
- Semico clean, ultrasound, 1 min.
- deionized H_2O rinse, 1 min.
- microscope check: look for resist adhesion problems.

iv. Calibrate etch rates on dummy samples:

- InGaAs - nom. etch rate: 2500Å/min.
- InAlAs - nom. etch rate: 3500Å/min.

v. mesa etch (perform first on expendable piece if possible):
etch in ultrasound at 25° for 6 min (20% overetch added) based on the following guidelines:

A. InGaAs - 24 sec. per 1000$\AA$ (nominal)

B. InAlAs - 17 sec. per 1000$\AA$ (nominal)

vi. Rinse in deionized H_2O, 1 min., twice.

vii. N_2 blow-dry.

viii. microscope inspection.

ix. If first run was on a dummy sample, repeat for real samples once satisfied.

(d) Remove PR:

i. acetone, ultrasound, 2 min.

ii. rinse briefly in methanol before acetone dries.

iii. deionized H_2O rinse, 1 min., N_2 blow dry.

iv. microscope inspection.

v. measure mesa heights on each sample:

Sample ID #	Mesa Height (Å)

3. Polyimide Passivation:

(a) Photolithography:

i. preparation:

A. check that pre-bake oven is on. Surface thermometer should read 110°C.

B. check that post-bake oven is on. Surface thermometer should read 160°C.

C. spray mask POLY with acetone/methanol, rinse with deionized H_2O, and N_2 blow dry to clean.

D. prepare adhesion promoter:
mix QZ 3289:QZ 3290 1:19 (5 ml : 95 ml) thoroughly; centrifuge if necessary.

ii. acetone, ultrasound, 2 min., twice.

iii. methanol, 1 min.

iv. deionized H_2O rinse, 1 min.

v. Semico clean, ultrasound, 1 min.

vi. deionized H_2O rinse, 1 min., and N_2 blow dry.

vii. dehydration bake, 110°C, 30 min.

viii. spin adhesion promoter, 4000 rpm, 20 sec.

ix. hot-plate bake, 110°C, 20 sec.

x. spin Probimide 408, photosensitive polyimide, 4000 rpm, 20 sec. (nominal thickness: 0.9 μm)

xi. heat in pre-bake oven, 110°C, 30 min.

xii. cool down 5 min.

xiii. test expose dummy samples, mask POLY (Estimate: 19 sec on ST, SOFT CONT).

xiv. develop with QZ 3301, 110 s; rinse with QZ 3312, 40s and N_2 blow dry.

xv. microscope inspection.

Previous data on p. ________ Power = ________ W
Intensity = ________ mW/cm^2

Sample ID #						
exp. time						
over/under						
alignment						
comments						

xvi. expose, develop, and inspect device samples.

Previous data on p. ________ Power = ________ W
Intensity = ________ mW/cm^2

Sample ID #						
exp. time						
over/under						
alignment						
comments						

xvii. heat in post-bake oven, 160°C, 2 hrs.

xviii. measure polyimide heights on each sample:

Sample ID #	Polyimide Height (Å)

4. Electrode Deposition using Conventional Photolithography:

   (a) Photolithography:

      i. preparation:

         A. check that pre-bake oven is on, and set at 90°C.

         B. check that post-bake oven is on, and set at 120°C.

         C. spray mask METAL with acetone/methanol, rinse with deionized H_2O, and N_2 blow dry to clean

      ii. Semico clean, ultrasound, 1 min.

iii. deionized H_2O rinse, 1 min.
iv. N_2 blow dry.
v. spin promoter, HMDS, 4000 rpm, 30 sec.
vi. spin resist, AZ 5214-E, 5000 rpm, 30 sec. (nominal thickness: 1.2 μm)
vii. heat in pre-bake oven, 90°C, 30 min.
viii. cool down 5 min.
ix. test expose dummy samples, mask METAL (Estimate: 8 cycles; each with a 2 sec long exposure and a 4 sec wait on ST, SOFT CONT)
x. heat in post-bake oven, 120°C, 90 sec.
xi. flood expose, 90 sec.
xii. develop in AZ422-MIF, 155 sec.
xiii. microscope inspection.

Previous data on p. ________ Power = ________ W
Intensity = ________ mW/cm^2

Sample ID #						
exp. time						
over/under						
alignment						
comments						

xiv. expose, develop, and inspect device samples.

Previous data on p. ________ Power = ________ W
Intensity = ________ mW/cm^2

Sample ID #						
exp. time						
over/under						
alignment						
comments						

(b) Clean and metal evaporation:

i. descum in plasma asher to etch 200Å of resist:
Power = 200 W, Time = 45 $sec.$
Loading =_____, Tuning =_____
ii. deionized H_2O rinse, 1 min.

iii. Semico, ultrasound, 1 min.
iv. deionized H_2O rinse, 1 min.
v. N_2 blow dry.
vi. evaporate 3000 $\AA$ of Pt/Ti/Au (50/200/2750 $\AA$)

(c) Lift-off:

i. immerse in acetone, ultrasound, 1 min., twice.
ii. deionized H_2O rinse, 1 min., and N_2 blow dry.
iii. microscope inspection.

5. Electrode Deposition using X-ray Lithography

(a) X-ray lithography:

i. preparation:
A. check that pre-bake oven is on, and set to 180°C.
B. spray mask METAL with acetone/methanol, rinse with deionized H_2O, and N_2 blow dry to clean.
C. prepare a 4:6 MIBK:IPA developing solution.
ii. acetone, ultrasound, 2 min., twice.
iii. methanol, 1 min.
iv. deionized H_2O rinse, 1 min.
v. Semico clean, ultrasound, 1 min.
vi. deionized H_2O rinse, 1 min., and N_2 blow dry.
vii. spin resist, KTI PMMA 950K 4% 4220 rpm, 60 sec. (nominal thickness = 0.25 μm.)
viii. heat in pre-bake oven, 180°C, 1 hr.
ix. cool down 5 min.
x. test expose dummy samples, mask METAL (Estimate: 7 hrs)
Dose: 1 KJ/cm^3 and Source-substrate distance: 10 cm.
xi. develop using 4:6 MIBK:IPA, 1 min.
xii. rinse with IPA, 30 sec and N_2 blow dry.
xiii. microscope inspection.

Previous data on p. ________ Power = ________ W
Intensity = ________ mW/cm^2

Sample ID #						
exp. time						
over/under						
alignment						
comments						

xiv. expose, develop and inspect device samples.

Previous data on p. ________ Power = ________ W
Intensity = ________ mW/cm^2

Sample ID #						
exp. time						
over/under						
alignment						
comments						

(b) Clean and metal evaporation:

i. descum in UV ozone for 2 min to remove 200$\AA$
ii. deionized H_2O rinse, 1 min.
iii. Semico, ultrasound, 1 min.
iv. deionized H_2O rinse, 1 min.
v. N_2 blow dry.
vi. evaporate 1200 $\AA$ of Pt/Ti/Pt/Au (50/200/250/700 $\AA$)

(c) Lift-off:

i. immerse in acetone, ultrasound, 1 min., twice.
ii. deionized H_2O rinse, 1 min., and N_2 blow dry.
iii. microscope inspection.

6. Contact Pad Reinforcement:

(a) Photolithography:

i. preparation:

A. check that pre-bake oven is on, and set at 90°C.
B. check that post-bake oven is on, and set at 120°C.
C. spray mask PASS with acetone/methanol, rinse with deionized H_2O, and N_2 blow dry to clean

ii. Semico clean, ultrasound, 1 min.
iii. deionized H_2O rinse, 1 min.
iv. N_2 blow dry.
v. spin promoter, HMDS, 4000 rpm, 30 sec.
vi. spin resist, AZ 5214-E, 5000 rpm, 30 sec. (nominal thickness: 1.2 μm)
vii. heat in pre-bake oven, 90°C, 30 min.
viii. cool down 5 min.
ix. test expose dummy samples, mask PASS (Estimate: 2.5 - 3 sec on ST, SOFT CONT)
x. heat in post-bake oven, 120°C, 90 sec.
xi. flood expose, 90 sec.
xii. develop in AZ422-MIF, 155 sec.
xiii. microscope inspection.

Previous data on p. ________ Power = ________ W
Intensity = ________ mW/cm^2

Sample ID #						
exp. time						
over/under						
alignment						
comments						

xiv. expose, develop, and inspect device samples.

Previous data on p. ________ Power = ________ W
Intensity = ________ mW/cm^2

Sample ID #						
exp. time						
over/under						
alignment						
comments						

(b) Clean and metal evaporation:

i. descum in plasma asher to etch 200Å of resist:
Power = 200 W, Time = 45 *sec.*
Loading =_____, Tuning =_____

ii. deionized H_2O rinse, 1 min.
iii. Semico, ultrasound, 1 min.
iv. deionized H_2O rinse, 1 min.
v. N_2 blow dry.
vi. evaporate 2500 $\mathring{A}$ of Au

(c) Lift-off:

i. immerse in acetone, ultrasound, 1 min., twice.
ii. deionized H_2O rinse, 1 min., and N_2 blow dry.
iii. microscope inspection.

Bibliography

[1] P. Bhattacharya, *Semiconductor Optoelectronic Devices*, Prentice Hall, Englewood Cliffs, NJ., 1994.

[2] J. Senior, *Optical Fiber Communications, Principles and Practice*, Prentice Hall series in Optoelectronics, 1985.

[3] J. B. D. Soole and H. Schumacher, "Transit-time limited frequency response of InGaAs MSM photodetectors," *IEEE Trans. Electron Devices*, vol. 37, no. 11, pp. 2285-2291, 1990.

[4] S. Miura, O. Wada, H. Hamaguchi, M. Ito, M. Makiuchi, K. Nakai, and T. Sakurai, "A monolithically integrated AlGaAs/GaAs p-i-n/FET photoreceiver by MOCVD," *IEEE Electron Device Lett.*, vol. EDL-4, pp. 375-376, 1983.

[5] R. M. Kolbas, J. Abrokwah, J. K. Carney, D. H. Bradshaw, B. R. Elmer, and J. R. Biard, "Planar monolithic integration of a photodiode and a GaAs preamplifier," *Appl. Phys. Lett.* vol. 43, pp. 821-823, 1993.

[6] S. Miura, H. Machida, O. Wada, K. Nakai, and T. Sakurai, "Monolithic integration of a pin photodiode and a field-effect transistor using a new fabrication technique - Graded step process," *Appl. Phys. Lett.*, vol. 46, pp. 389-391, 1985.

[7] J. D. Crow, C. J. Anderson, S. Bermon, A. Callegari, J. F. Ewen, J. D. Feder, J. H. Greiner, E. P. Harris, P. D. Hoh, H. J. Hovel, J. H. Magerlein, T. E. Mckoy, A. T. S. Pomerene, D. L. Rogers, G. J. Scott, M. Thomas, G. W. Mulvey, B. K.

Ko, T. Ohashi, M. Scontras, and D. Widiger, "A GaAs MESFET IC for optical multiprocessor networks," *IEEE Trans. Electron Devices*, vol. 36, p. 263, 1989.

[8] J. B. D. Soole and H. Schumacher, "InGaAs metal-semiconductor-metal photodetectors for long wavelength optical communications," *IEEE J. Quantum Electron.*, vol. 27, pp. 737-752, 1991.

[9] O. Wada, H. Hamaguchi, M. Makiuchi, T. Kumai, M. Ito, K. Nakai, T. Horimatsu, and T. Sakurai, "Monolithic four-channel photodiode/amplifier receiver array integrated on a GaAs substrate," *Journal of Lightwave Tech.*, vol. LT-4, pp 1694-1703, 1986.

[10] C. S. Harder, B. van Zeghbroeck, H. Meier, W. Patrick, and P. Vettiger, "5.2 GHz bandwidth monolithic GaAs optoelectronic receiver," IEEE Electron Device Lett., vol. 9, pp. 171-173, 1988.

[11] G. K. Chang, W. P. Hong, J. L. Gimlett, R. Bhat, and C. K. Nguyen, " High performance monolithic dual-MSM photodetector for long wavelength coherent receivers," *Electron. Lett.*, vol. 25, no. 16, pp. 1018-1023, 1989.

[12] R. J. Phelan, D. R. Larson, N. V. Frederick, and D. L. Frazen, "Submicrometer interdigital silicon detectors for the measurement of picosecond pulses," *Proc. SPIE*, vol. 439, pp. 207-211, 1983.

[13] A. M. Johnson, A. M. Glass, D. H. Olson, W. M. Simpson and J. P. Harbison, "High quantum efficiency amorphous silicon photodetectors with picosecond response times," *Appl. Phys. Lett.* vol. 44, pp. 450-452, 1984.

[14] B. W. Mullins, S. F. Soares, K. A. McArdle, C. W. Wilson, and S. R. J. Brueck, "A simple high-speed Si Schottky photodiode," *IEEE Photon. Tech. Lett.*, vol. 3, pp. 360-362, 1991.

[15] S. Y. Wang, and D. M. Bloom, "100 GHz bandwidth planar GaAs Schottky diode." *Electron. Lett.* vol. 19, pp. 554-555, 1983.

[16] M. Ito and O. Wada, "Low dark current GaAs metal-semiconductor-metal (MSM) photodiodes using WSi_x contacts," *IEEE J. Quantum Electron.*, vol. QE-22, no. 7, pp. 1073-1077, 1986.

[17] B. J. van Zeghbroeck, W. Patrick, J. M. Halbout, and P. Vettiger, "105 GHz bandwidth metal-semiconductor-metal photodiode," *IEEE Electron Device Lett.* vol. 9, pp. 171-173, 1988.

[18] T. Kikuchi, H. Ohno, and H. Hasegawa, "$In_{0.53}Ga_{0.47}As$ metal-semiconductor-metal photodiodes using a lattice matched AlGaAs Schottky assist layer," *Electron. Lett.*, vol. 24, pp. 1208-1210, 1988.

[19] J. B. D. Soole, H. Schumacher, H. P. Le Blanc, R. Bhat, and M. A. Koza, "High-speed performance of OMCVD grown InAlAs/InGaAs MSM photodetectors at 1.55 μm and 1.3 μm wavelength," *IEEE Photon. Tech. Lett.*, vol. 1, pp. 250-252, 1989.

[20] O. Wada, H. Nobuhara, H. Hamaguchi, T. Mikawa, A. Tackeuchi, and T. Fujii, "Very high speed GaInAs metal-semiconductor-metal photodiode incorporating an AlInAs/InGaAs graded superlattice," *Appl. Phys. Lett.*, vol. 54, pp. 16-17, 1989.

[21] E. H. Bottcher, D. Kuhl, F. Hieronymi, E. Droge, T. Wolf, and D. Bimberg, "Ultrafast semiinsulating InP:Fe-InGaAs:Fe-InP:Fe MSM photodetectors: modeling and performance," *IEEE J. Quantum Electron.*, vol. 28, no. 10, pp. 2343-2357, 1992.

[22] S. R. Nagel, "Optical Fiber - The Expanding Medium," *IEEE Circ. and Dev. Mag.*, p. 36 Mar. 89.

[23] G. I. Ng, W. P. Hong, D. Pavlidis, M. Tutt, P. K. Bhattacharya, "Characteristics of Strained $In_{0.65}Ga_{0.35}As/In_{0.52}Al_{0.48}As$ HEMT with Optimized Transport Parameters," *IEEE Electron Device Lett.* vol. 9, no. 9, p. 439, 1988.

[24] N. Shigekawa, T. Furuta, K. Arai, "Time-of-flight measurement of electron velocity in an $In_{0.52}Al_{0.48}As/In_{0.53}Ga_{0.47}As/In_{0.52}Al_{0.48}As$ double heterostructure," *J. Appl. Phys.*, vol. 57, no. 1, p. 67, 1990.

[25] D. M. Gvozdić, J. B. Radunovic, and J. M. Elazar, "An analytical expression for the electric field in MSM structures," *Int. J. Infrared and Millimeter Waves*, vol. 14, no. 7, pp. 1485-1493, 1993.

[26] W. C. Koscielniak, J. Pelouard, and M. A. Littlejohn, "Intrinsic and extrinsic response of GaAs metal-semiconductor-metal photodetectors," *IEEE Photon. Tech. Lett.*, vol. 2, no. 2, pp. 125-127, 1990.

[27] C. Moglestue, J. Rosenzweig, J. Kuhl, M. Klingenstein, M. Lambsdorff, A. Axmann, J. Schneider, and A. Hulsmann, "Picosecond pulse response characteristics of GaAs metal-semiconductor-metal (MSM) photodetectors," *J. Appl. Phys.*, vol. 70, pp. 2435-2448, 1991.

[28] Y. C. Lim and R. A. Moore, "Properties of alternately charged coplanar parallel strips by conformal mappings," *IEEE Trans. Electron Devices*, vol. ED-15, pp. 173-180, 1968.

[29] The 2-D Poisson simulator used for this work was written by Greg Snider, Applied and Engineering Physics Dept., Cornell University.

[30] A. Yariv, *Optical Electronics*, 3rd edition, chapter 10, pp. 315-316, 1985.

[31] W. C. Koscielniak, J. L. Pelouard, and M. A. Littlejohn, "Dynamic behavior of photocarriers in a GaAs metal-semiconductor-metal photodetector with sub-half-micron electrde pattern," *Appl. Phys. Lett.*, vol. 54, pp. 567-569, 1989.

[32] H. H. Wieder, "Fermi level and surface barrier of $Ga_xIn_{1-x}As$ alloys," *Appl. Phys. Lett.* vol. 38, no. 170, 1981.

[33] K. Kajiyama, Y. Mizushima, and S. Sakata, "Schottky barrier height of n-$In_xGa_{1-x}As$ diodes," *Appl. Phys. Lett.*, vol. 23, no. 8, p. 458, 1973.

[34] H. T. Griem, S. Ray, J. L. Freeman, and D. L. West, "Long wavelength (1.0 μm-1.6 μm) $In_{0.52}Al_{0.48}As/In_{0.53}(Ga_xAl_{1-x})_{0.47}As/In_{0.53}Ga_{0.47}As$ metal-semiconductor-metal photodetector," *Appl. Phys. Lett.*, vol. 56, pp. 1067-1068, 1990.

[35] L. Yang, A. S. Logan, R. A. Tanbun-Ek, and W. T. Tsang, "High performance Fe:InP/InGaAs metal/semiconductor/metal photodetector," IEEE Photon. Tech. Lett. vol. 2, pp. 58-61, 1990.

[36] A. Temmar, J. P. Praseuth, E. Legros, and A. Scavennec, "AlInAs/GaInAs metal-semiconductor-metal photodiode with very low leakage current and 4-element arrays," in *Proc. ECOC/IOOC '91*, Paris, France, Sept. 1991, pp. 273-276.

[37] W. P. Hong, G. K. Chang, and R. Bhat, "High performance $Al_{0.15}Ga_{0.85}As/In_{0.53}Ga_{0.47}As$ MSM photodetectors grown by OMCVD," *IEEE Trans. Electron Devices*, vol. 36, pp. 659-662, 1989.

[38] S. E. Ralph, M. C. Hargis, and G. D. Pettit, "Large area, low voltage, transit time limited InGaAs metal semiconductor metal photodetectors," *Appl. Phys. Lett.* vol. 61, no. 18, pp. 2222-2224, 1992.

[39] H. Schumacher, H. P. LeBlanc, J. Soole, and R. Bhat, "An investigation of the optoelectronic response of GaAs/InGaAs MSM photodetectors," *IEEE Electron Device Lett.* vol. 9, no. 11, pp. 607-609, 1988.

[40] M. Leibovitch, "Modeling of Semiconductor Interfaces", PhD. Thesis, Tel-Aviv University, July 1994.